



The 95% Confidence Interval for GNSS-Derived Site Velocities

Guoquan Wang, M.ASCE¹

Abstract: Linear trends, or site velocities, derived from global navigation satellite system (GNSS) positional time series have been commonly applied to site stability assessments, structural health monitoring, sea-level rise, and coastal submergence studies. The uncertainty of the velocity has become a big concern for stringent users targeting structural or ground deformation at a few millimeters per year. GNSS-derived positional time series are autocorrelated. Consequently, conventional methods for calculating the standard errors of the linear trends result in unrealistically small uncertainties. This article presents an approach to accounting for the autocorrelation with an effective sample size (N_{eff}). A robust methodology has been developed to determine the 95% confidence interval (95%CI) for the site velocities. It is found that the 95%CI fits an inverse power-law relationship over the time span of the time series (vertical direction: 95%CI = $5.2T^{-1.25}$; east–west or north–south directions: 95%CI = $1.8T^{-1.0}$). For static GNSS monitoring projects, continuous observations longer than 2.5 and 4 years are recommended to achieve a 95%CI below 1 mm/year for the horizontal and vertical site velocities, respectively; continuous observations longer than 7 years are recommended to achieve a 95%CI below 0.5 mm/year for the vertical land movement rate (subsidence or uplift). The 95%CI from 7-year GNSS time series is equivalent to the 95%CI of the sea-level trend derived from 60-year tide gauge observations. The method and the empirical formulas developed through this study have the potential for broad applications in geosciences, sea-level and coastal studies, and civil and surveying engineering. DOI: [10.1061/\(ASCE\)SU.1943-5428.0000390](https://doi.org/10.1061/(ASCE)SU.1943-5428.0000390). © 2021 American Society of Civil Engineers.

Author keywords: Autoregressive model; Effective sample size; Global navigation satellite system (GNSS); Linear trend; Site velocity; Sea-level rise; Uncertainty; 95% confidence interval.

Introduction

Motivation

Static global navigation satellite system (GNSS) monitoring techniques have been increasingly applied in long-term geological hazards (e.g., subsidence, landslides, faulting) and structural health monitoring. Most applications do not directly use the absolute positions but rely on the change of positions over a specific time range, that is, site velocity. Accurate site velocities are needed in assessing long-term site stability and structural deformation. However, a site velocity must be used only with a full understanding of its uncertainty.

In the sea-level research community, the 95% confidence interval (95%CI) is used as a standard index to assess the uncertainty or reliability of tide gauge (TG)–derived mean sea-level change rates. The National Ocean Service (NOS) Center for Operational Oceanographic Products and Services (CO-OPS) at the National Oceanic and Atmospheric Administration (NOAA) routinely processes TG data along the US coasts and publishes the relative sea-level trends and their corresponding 95%CI (e.g., Zervas et al. 2013). The NOAA products have been widely applied in the sea-level and coastal research communities. During the past two decades, closely spaced GNSS and TG data sets have been routinely applied

to derive sea-level rise rates with respect to global or regional reference frames (e.g., Snay et al. 2007; Santamaría-Gómez et al. 2012; Zhou et al. 2021). The sea-level research and coastal engineering communities urgently need a consistent method to estimate the 95%CI of the trends of vertical land movements (VLMs). This motivates development of a general methodology for determining the 95%CI of the GNSS-derived site velocities.

GNSS has become the standard generic term for satellite navigation systems in the satellite positioning community, including the United States' GPS, Russia's GLONASS, Europe's Galileo, China's Beidou, and other regional satellite navigation systems. This investigation only used GPS signals in calculating daily static positions. The methodology developed through this study is applicable to the daily positional time series derived from other satellite systems, however. Accordingly, I use the umbrella term *GNSS* throughout this article.

Common Problems

An ordinary linear regression is often used to estimate the linear trend from GNSS-derived displacement time series (or relative positions). Though slightly different approaches are used in implementing the least squares by various researchers, they all result in very similar site velocity estimates (linear trends) for sites naturally experiencing linear movements over time. However, the uncertainties of GNSS-derived site velocities reported by different researchers could be considerably different.

In statistics, there are sophisticated mathematical methods for calculating the linear trend and its uncertainty, also known as standard error, for stationary time series. A stationary time series is one whose statistical properties such as mean, variance, and autocorrelation do not depend on the time at which the series is measured. The commonly used form of linear regression is called ordinary

¹Professor, Dept. of Earth and Atmospheric Sciences, Univ. of Houston, Houston, TX 77204. ORCID: <https://orcid.org/0000-0003-3731-3839>. Email: gwang@uh.edu

Note. This manuscript was submitted on March 30, 2021; approved on September 30, 2021; published online on November 18, 2021. Discussion period open until April 18, 2022; separate discussions must be submitted for individual papers. This paper is part of the *Journal of Surveying Engineering*, © ASCE, ISSN 0733-9453.

least-squares regression. This study employs the ordinary linear regression methods commonly used in the broad geophysical sciences (e.g., Wilks 2006, Chapter 6). Assuming y_i is the GNSS-derived daily displacement time series with respect to a specific reference frame, a simple linear regression can be used to model the daily positional time series

$$y_i = a + bt_i + R_i \quad (1)$$

where a = Y -intercept of the regression line (usually just called the intercept); b = slope of the linear regression; t_i = series of Julian days with the unit of fractional years (e.g., May 1, 2020, is counted as $2,020 + 121.5/365.25 = 2,020.3326$ years); and R_i = residual time series. The coefficient of correlation between t_i and y_i ($i = 1, N$) is defined as

$$r_{ty} = \frac{\sum_{i=1}^N [(t_i - \bar{t})(y_i - \bar{y})]}{\sqrt{\sum_{i=0}^N (t_i - \bar{t})^2 \sum_{i=0}^N (y_i - \bar{y})^2}} \quad (2)$$

where \bar{t} and \bar{y} = mean values of the time series t_i and y_i , respectively. The coefficients (a, b) and their standard errors are obtained as follows:

$$b = r_{ty} \times \frac{\sigma_y}{\sigma_t} \quad (3)$$

$$a = \bar{y} - b \times \bar{t} \quad (4)$$

where σ_t and σ_y = standard deviation of the series of t_i and y_i . The residual time series can be obtained by

$$R_i = a + bt_i - y_i \quad (5)$$

The standard error of the regression, which is represent by s , can be obtained by

$$s = \sqrt{\frac{\sum_{i=1}^N R_i^2}{N - 2}} \quad (6)$$

where s represents unbiased estimate of the standard deviation of the residual time series. For time series with hundreds to thousands of samples, s is the same as the RMS of the residuals ($\text{RMS} = \sqrt{(\sum_{i=1}^N R_i^2)/N}$), which is often used to assess the repeatability (also called RMS accuracy) of GNSS positioning (Soler and Wang 2016). The standard error of s is defined as

$$\text{SE}_s = \frac{s}{\sqrt{N}} \quad (7)$$

where SE_s is measured in the units of y centimeters or millimeters for the GNSS-derived displacements. The standard error of the slope b is estimated by a further adjustment of SE_s

$$\text{SE}_b = \frac{s}{\sqrt{N}} \times \frac{1}{\sigma_t} \quad (8)$$

where $1/\sigma_t$ merely serves to scale the value and unit of SE_s ; and σ_t represents standard deviation of the series of observational days (t_i) in decimal years. The units of SE_b is consistent with the units of the slope (b). For t_i series with a time span of T years (e.g., $T > 1$ year), $\sigma_t \approx T/(2\sqrt{3})$.

If the residual time series (R_i) is stationary, SE_s does a good job representing the uncertainty of the linear regression, and SE_b does a good job representing the uncertainty of the slope (b). However, the residual time series (R_i) from GNSS observations is not stationary. It often exhibits trends, seasonality, random walking, and other nonstationary behaviors, known as power-law noise in general

(e.g., Agnew 1992; Langbein and Johnson 1997; Williams et al. 2004). Temporal-correlated errors are pervasive in GNSS-derived displacement time series, in both horizontal and vertical directions. Error terms correlated over time or space are said to be autocorrelated. Autocorrelation has been investigated in the geodetic community since the late 1960s, first discovered by Krarup (1969) and expanded and explained by Moritz (1973) for gravity predictions. For the GNSS time series, the position of each day is partially correlated with the position values of the previous and following days. Therefore, there are actually many fewer independent measurements contributing to the standard error of the linear regression. Consequently, SE_b calculated using the total sample number N is unrealistically small. Fig. 1 illustrates the three-component displacement time series at THSU (2013–2020). The antenna of THSU is mounted on the sidewall of a 1-story laboratory building at the University of Houston (UH) [Fig. 2(a)]. The reference frame of the displacement time series is the International GNSS Service Reference Frame 2014 (IGS14) (Altamimi et al. 2016; Rebischung et al. 2016). The value of SE_b equals 0.02 mm/year for each horizontal velocity [east–west (EW) or north–south (NS)] and 0.05 mm/year for the vertical velocity. Usually, these estimates below 0.1 mm/year are unrealistically small and significantly underestimate the real uncertainties of linear trends.

Current Approaches

Trend estimation is a common task in the geophysical research and application community. In parallel, the GNSS geodetic research community has developed two approaches for obtaining realistic uncertainty estimates of GNSS-derived site velocities. One is the scaling approach, and another is the noise-modeling approach.

Approach 1: Scaling

In order to make the calculated velocity uncertainty (SE_b) more realistic and reasonable, one or more scale factors are often applied to correct (increase) SE_b in practice. The scale factors used in geodesy literature vary widely from 2 to 20 (e.g., Dixon et al. 2000; Bettinelli et al. 2006; Heflin et al. 2020). Consequently, it is hard to align the uncertainties published by different research groups, though each group may provide consistent uncertainty estimates for their own velocity products.

The geodetic research groups at the Jet Propulsion Laboratory (JPL) of the National Aeronautics and Space Administration (NASA) and Nevada Geodetic Laboratory (NGL) of the University of Nevada, Reno, routinely process global GNSS data and provide daily precise point positioning (PPP) solutions and their velocity products to the research community (Blewitt et al. 2018; Heflin et al. 2020). Both JPL and NGL employ the GipsyX software package for static GNSS processing (Bertiger et al. 2020). The PPP solutions with respect to regional reference frames have attracted broad interest in natural hazard studies (earthquakes, landslides, subsidence, volcanoes) (e.g., Wang et al. 2014; Murray and Svart 2017) and long-term structural deformation monitoring because of the simplicity in the data process and the consistency of positional accuracy over time and space (e.g., Bao et al. 2018; Guo et al. 2019; Zhao et al. 2020). JPL applies a single factor of 20 for correcting the uncertainty of the whole time series (Heflin et al. 2020). NGL employs the Median Interannual Difference Adjusted for Skewness (MIDAS) method in calculating the site velocities and corresponding uncertainties (Blewitt et al. 2016). MIDAS uses the median of slopes of a great number of selected 1-year-apart displacements to represent the overall site velocity. The standard deviation of these slopes somehow reflects the uncertainty of the selected velocity. However, the unscaled standard deviation is unrealistically small because of the temporal correlation among

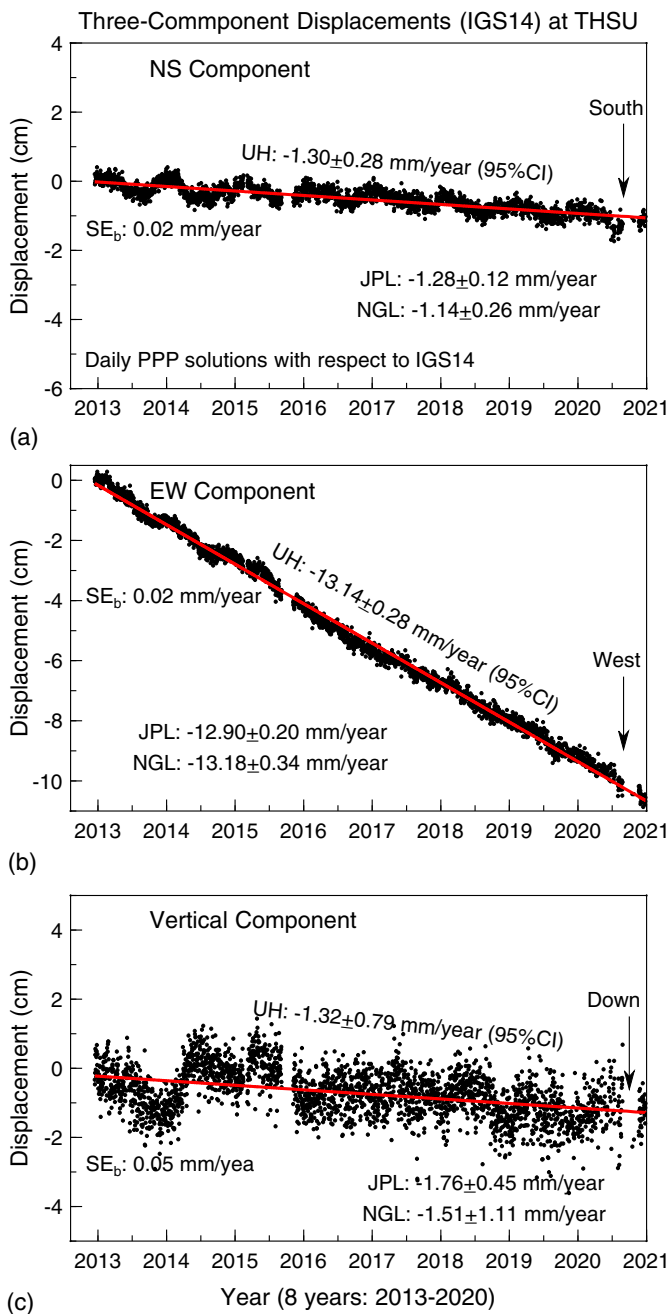


Fig. 1. Three-component displacement time series at GNSS site THSU at UH: (a) NS direction; (b) EW direction; and (c) vertical direction. The site velocities and their uncertainties (as of January 20, 2021) published by Jet Propulsion Laboratory (JPL 2021) and Nevada Geodetic Laboratory (NGL 2021) are marked on each subplot. The UH results, site velocity, and its 95%CI are obtained according to Eq. (16), and SE_b is obtained according to Eq. (8).

the GNSS observations. MIDAS further corrects the calculated standard deviation by scaling.

For site THSU illustrated in Fig. 1, the site velocities and their uncertainties reported by JPL and NGL (JPL 2021; NGL 2021), as well as the results from this study, are marked on each subplot. It appears that JPL and NGL velocities and their corresponding uncertainties are comparable in the NS and EW directions. Both result in 0.2 to 0.3 mm/year velocity uncertainties. However, the vertical uncertainties are considerably different. The JPL results show an

uncertainty of 0.45 mm/year, while the NGL results show an uncertainty of 1.11 mm/year. The UH results are obtained according to the method introduced in this article. For structural monitoring looking at deformations of a few millimeters per year level, uncertainties at a level of submillimeter per year (<1 mm/year) are often required; for sea-level and coastal submergence studies, uncertainties below 0.5 mm/year are often required. The main reason causing the difference of the uncertainties among the JPL and NGL results is the scale factors that they used. This study aims to develop a general methodology for determining the uncertainties of GNSS-derived site velocities without involving scaling factors.

Approach 2: Noise Modeling

Over the past three decades, the geodetic research community has developed a number of methods for modeling the noise contents superimposed onto the GNSS daily time series, thus improving the estimates of the linear trend and its uncertainty, particularly the uncertainty. In general, the noises can be modeled by a combination of white noise and power-law noise (Agnew 1992; Langbein 2004), including white noise, flicker noise, random-walk noise, and their combinations (e.g., Zhang et al. 1997; Mao et al. 1999; Hackl et al. 2011; Langbein 2008; Wang et al. 2012). White noise represents temporally uncorrelated phenomena; flicker noise often includes mismodeled parameters during data processing, as well as large-scale effects; random-walk noise is often dominated by site-dependent effects and monument instability (e.g., Williams et al. 2004; Williams 2008; Langbein 2012; Klos et al. 2014; Ray et al. 2019). Those modeling methods have been employed in routine GNSS time series processing, such as the UNAVCO GAGE Network processing (Herring et al. 2016), the CATS program (Williams 2008), and the Hector program (Bos et al. 2013). The CATS and Hector programs estimate both the linear trend and the parameters of the chosen noise model primarily using the maximum likelihood estimation (MLE) method, which is an iterative minimization process. MLE requires computing the inverse of the covariance matrix in each step and thus often brings along a computationally inefficient problem (Langbein 2017). The uncertainty of the linear trend is further estimated using the information provided by the final data covariance matrix and empirical relationships, such as those found in Zhang et al. (1997) and Mao et al. (1999). Essentially, the accuracy or reliability of the velocity uncertainty largely depends on the goodness of the fitting models. It is always a challenge to precisely model the site-specific component of the GNSS noises.

This study does not attempt to dig into the details of the noises and modeling, but instead focuses on modeling the autocorrelation among the GNSS daily displacement measurements. The autocorrelation would provide essential information for estimating the size of independent GNSS measurements, and thus provide an analytical approach to calculating the velocity uncertainty.

Methodology

Decomposition of GNSS Time Series

Long-period nonlinear motions and periodical motions are the major contributions to the autocorrelation within the GNSS time series. To exclude those known correlations, the GNSS-derived displacement time series is decomposed into four components: a linear trend, a nonlinear trend, a seasonal trend, and residuals. The linear, nonlinear, and seasonal motions are regarded as the deterministic parts, while the residuals are regarded as the noise part. Both the deterministic and noise parts could contribute to the uncertainty of the overall linear trend. The noise superimposed onto the GNSS time series could be induced by many causes, such as unmodeled

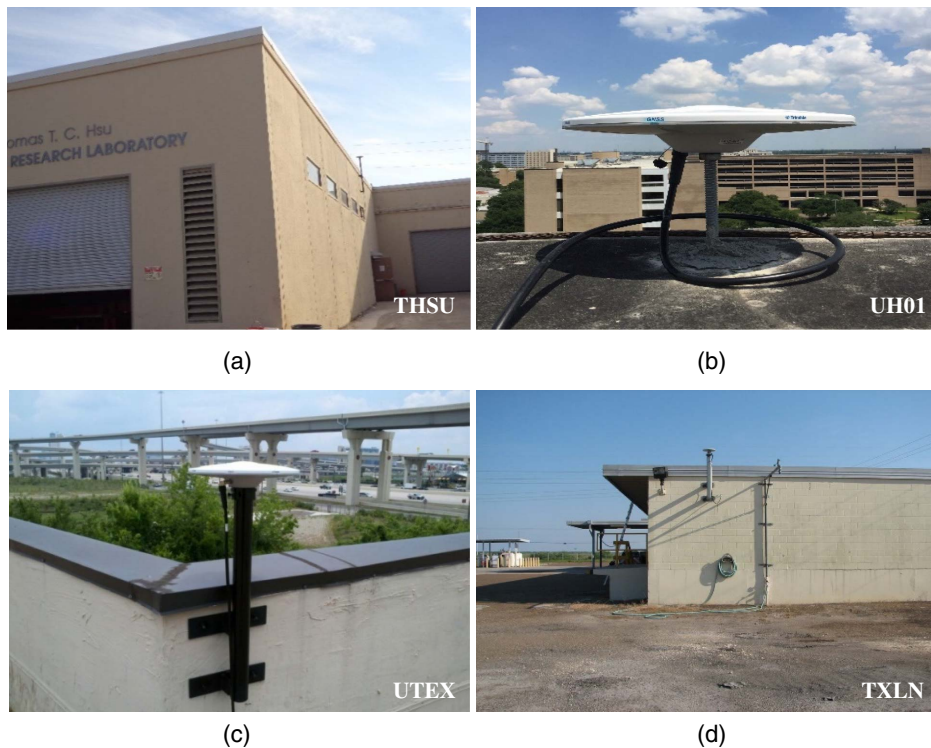


Fig. 2. Field installation of GNSS antennas whose positional time series are illustrated in this article: (a) THSU; (b) UH01; (c) UTEX; and (d) TXLN [image courtesy of the Continuously Operating Reference Station (CORS) website operated by the National Geodetic Survey (NGS), NOAA].

true physical site motion generated by surface loading due to hydrology and atmospheric pressure, effects of multipath, instability of antenna monuments, and errors in modeling satellite orbits and the Earth orientation parameters (e.g., Blewitt and Lavallee 2002; Griffiths and Ray 2009; King and Williams 2009).

The first step of the decomposition process is to calculate the linear trend (L_i) with the ordinary least-squares regression over the entire time series. The second step is to decompose the de-linear-trended time series into three components: a smoothed nonlinear trend (NL_i), a seasonal trend (S_i), and a residual time series (r_i). So, the displacement time series y_i ($i = 1, N$) can be described as

$$y_i = L_i + NL_i + S_i + r_i \quad (9)$$

where $L_i = a + bt_i$, with b being the linear trend [Eq. (3)] and a being the intercept of the linear trend [Eq. (4)]. I use the classical moving regression method called locally weighted scatterplot smoothing (LOWESS) (Cleveland 1981) to capture the nonlinear trend (NL_i). LOWESS uses a nonparametric technique to fit a smooth curve through points in a scatterplot. A smoothing parameter is designed to control the smoothness of the curve. The smoothing parameter, a value in $(0, 1)$, decides the proportion of observations to use for local regression. A larger value of the smoothing parameter results in a smoother curve, and a smaller value captures more short-period signals. The smoothing parameter is set as 0.4 in this study, which works well for the purpose of capturing the long-period (>2 years) trends.

Fig. 3 illustrates the steps for decomposing the displacement time series at UH01 (2013–2019). The displacements are referred to the stable Gulf of Mexico Reference Frame 2020 (GOM20), which was realized by 55 long-term GNSS stations (13.5 years on average) located within the inland of the Gulf of Mexico (GOM) coastal plain (Wang et al. 2020). The GNSS antenna (UH01) is mounted on the roof of the 7-story building in which the Department of Earth and

Atmospheric Sciences at the University of Houston is located [Fig. 2 (b)]. Typically, there are certain data gaps in continuous GNSS observations, often caused by the temporary failure of field equipment (antenna, receiver, power supplies) (Yang et al. 2016). The decomposing process requires continuous time series if the fast Fourier transform (FFT) is employed to analyze the seasonality. I use the classical hot-deck imputation to fill in the missing data in this study. Ford (1983) provides an introduction of the method. The idea of the hot-deck method is simple: borrow (in a random way) information from a set of nearby observations (the donor) to fill the missing information. In my implementation, each missing-data slot is flagged. A loop is performed to fill the empty slots one by one. For each flagged slot, the program finds the location of the nearest unflagged point. The distance is called D . The program takes the nearest $D + 5$ unflagged points before and after the flagged one to compute the weighted mean of these neighbors and fills the missing slot with the mean value. More neighboring observations are used for filling large gaps than small gaps. The random weights are generated by a Gaussian random number generator. The potential impacts of data gaps on the 95%CI will be discussed in the next section.

Seasonal signals are primarily caused by periodical surface mass redistribution (atmosphere, hydraulic, ocean, snow, and soil moisture) and bedrock thermal expansion (e.g., Dong et al. 2002). In general, the seasonal component (S_i) can be modeled by a combination of annual and semiannual cycles. On physical grounds, the amplitudes and phases of the seasonal signals may vary over time because the sources of the seasonal signals are not constant. Advanced models and methods have been developed to consider the time-varying amplitudes and phases of seasonal signals, such as the singular spectrum analysis method (e.g., Chen et al. 2013; Xu and Yue 2015), the Kalman filter method (e.g., Davis et al. 2012; Didova et al. 2016), the wavelet decomposition method (e.g., Bogusz 2015), the MLE (e.g., Langbein 2004; Bos et al. 2013), and the moving ordinary least-squares method (Klos et al. 2018). In

Decomposition of GNSS-Derived Displacement Time Series: UH01 (Reference Frame: GOM20)

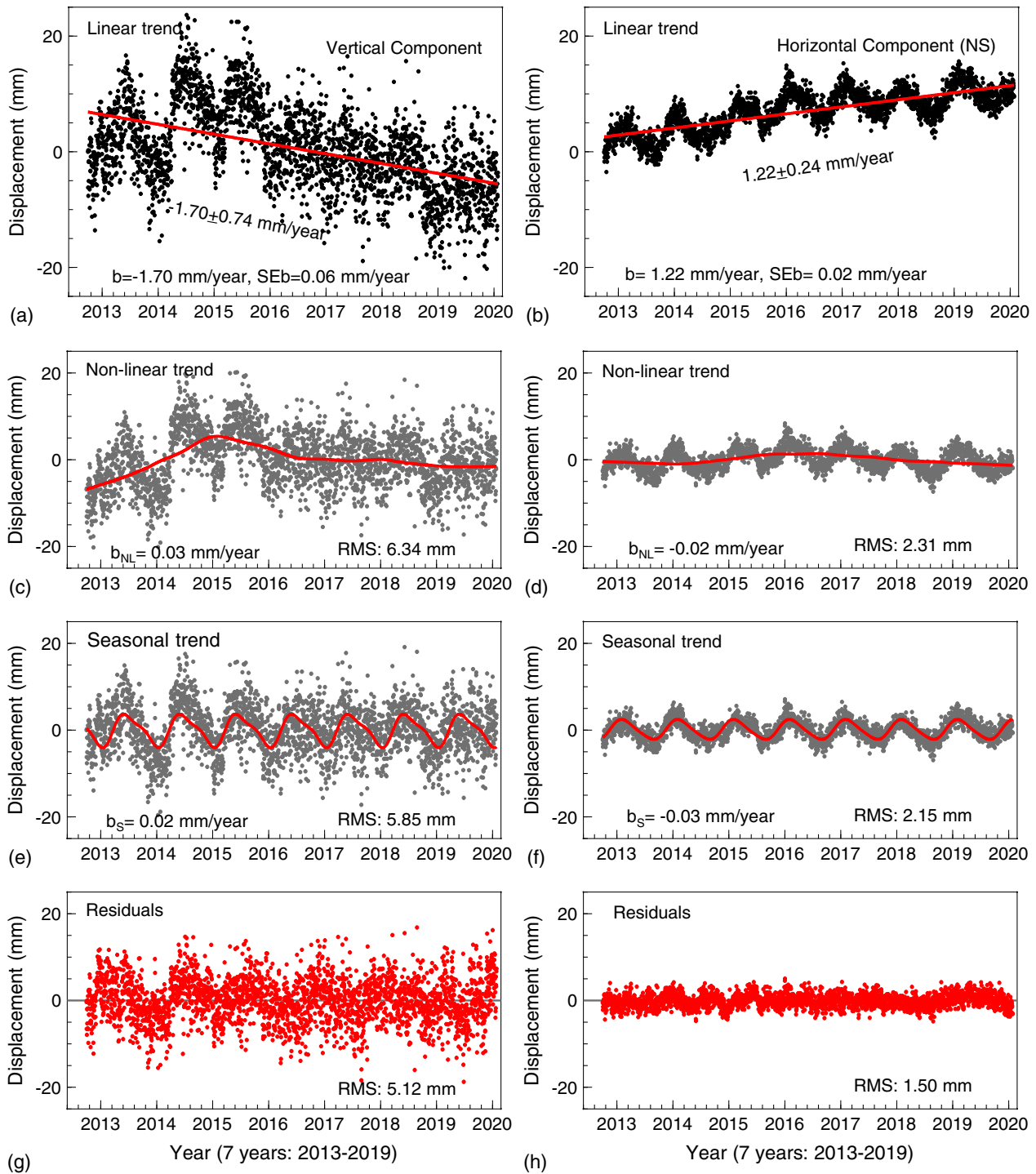


Fig. 3. Decomposition of the GNSS-derived displacement time series at UH01: (a and b) linear trends of the vertical and NS components, respectively; (c and d) nonlinear components of the vertical and NS components, respectively; (e and f) seasonal trends of the vertical and NS components, respectively; and (g and h) residuals of the vertical and NS component, respectively. RMS = root-mean square of each time series; b = linear trend of the original time series; S_b = standard error of the linear trend [Eq. (8)]; b_{NL} = linear trend of the nonlinear component [NL_i , Eq. (9)]; and b_S = linear trend of the seasonal component [S_i , Eq. (9)].

this study, I model the seasonal ground motions with a sum of annual and semiannual sinusoids with constant amplitudes and phases

$$S(t_i) = c_1 \cos(2\pi \times t_i) + d_1 \sin(2\pi \times t_i) + c_2 \cos(4\pi \times t_i) + d_2 \sin(4\pi \times t_i) \quad (10)$$

where t_i = epoch (observation day) with a unit in decimal years; and c_1, d_1, c_2 , and d_2 = coefficients deciding the amplitudes of the annual and semiannual signals. The seasonal information that is not properly modeled by the seasonal model [Eq. (10)] will be captured by the residual time series [r_i , Eq. (9)] as noise. The coefficients c_1, d_1, c_2 , and d_2 can be estimated by using the least-squares fitting methods

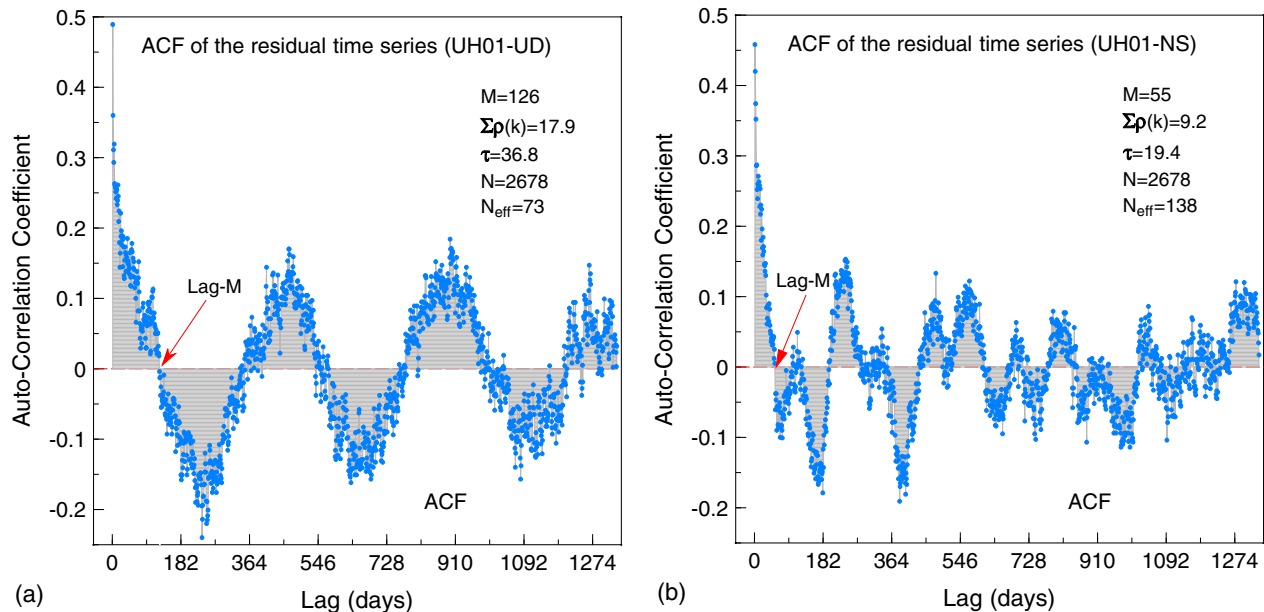


Fig. 4. ACF of the residual time series of the (a) vertical (up–down); and (b) horizontal (NS) components of UH01. N = number of total measurements; quantities M , $\sum \rho_k$, τ , and N_{eff} are defined in Eqs. (13) and (14), and discussions thereafter.

(e.g., Bos et al. 2013) or by using FFT. In my program, I employ the FFT method that computes the discrete Fourier transform of the residual time series. In the method, c_1 and d_1 are the Fourier coefficients of 1-year-period signals; and c_2 and d_2 are the Fourier coefficients of half-year-period signals.

Effective Sample Size

As mentioned previously, the autocorrelation among the adjacent GNSS measurements causes the extremely small standard error (SE_b) of the estimated slope [Eq. (8)]. The number of independent measurements is much fewer than the number (N) of total measurements. In theory, only the number of independent samples should be used to calculate the standard error (SE_b). *Effective sample size* (N_{eff}) is a term used in statistics to represent the independent samples among autocorrelated time series (e.g., Kass et al. 1998). The value of N_{eff} can be estimated by modeling the residual time series (R_i) using an autoregressive (AR) model, a linear regression predicting a coming value based on previous values from the same time series. A lag- p -order autoregressive model AR(p) can be described as

$$R_i = \varphi_0 + \varphi_1 R_{i-1} + \varphi_2 R_{i-2} + \dots + \varphi_p R_{i-p} + \varepsilon_i \quad (11)$$

where φ_k = partial autocorrelation function (PACF) of the residual time series (R_i) at lag k ; $\text{PACF}(k) = \varphi_k$; $\varphi_k \approx 0$ for $k > p$; and ε_i = white noise, the unpredictable component of R_i .

Autocorrelation function (ACF) and PACF are two primary tools for assessing the correlations among observations (e.g., Box et al. 2008). ACF describes how well the present value of the series is related to its past values. PACF shows the correlation of a series with itself at increasing lags after the correlations at the intervening lags have been removed. PACF is useful for identifying the order of an autoregressive model. The order is the number of immediately preceding values in the series used to predict the value at the present time. Partial autocorrelation coefficients that are significantly different from zero indicate lagged terms of the AR process that are useful for predicting R_i . Fig. 4 illustrates ACF of the residual time series of UH01 (vertical and NS) depicted in Figs. 3(g and h).

ACF exhibits a gradual decay toward zero at the first few lags, then fluctuates around the zero-axis. The overall decaying of ACF reflects the generally weaker statistical relationships between positions further away from each other in time. Fig. 5 depicts the PACF of the residual time series of UH01 (vertical and NS).

NOAA employs a first-order autoregressive model AR(1), or Markov, to model the residuals of the sea-level time series (Zervas 2009). An AR(1) model is a linear model that predicts the present value of a time series using the immediately prior value in time [Eq. (11)]. For an AR(1) process, the persistence of the effective sample size can be estimated using the approximation (Wilks 2006, p. 144)

$$N_{\text{eff}} \approx \frac{1 - \rho^2}{1 + \rho^2} \times N \quad (12)$$

where N = total sample size; N_{eff} = effective sample size; and ρ^2 = lag-1 autocorrelation coefficient. The values of ACF and PACF are the same at lag-1. Fig. 5 indicates that the maximum PACF is below 0.5 at UH01. PACF values at lag-2, lag-3, and lag-4 are noteworthy compared to the PACF at lag-1. Even the PACF below the 95% confidence intervals shown by the dashed lines are also statistically unignorable. Therefore, an AR(1) process is not the best for modeling the daily GNSS residual time series. A high-order AR model is needed. For a high-order autoregressive process [Eq. (11)], the effective sample size (N_{eff}) can be estimated by the following equations (e.g., Straatsma et al. 1986; Geyer 1992; Thompson 2010):

$$N_{\text{eff}} \approx \frac{N}{\tau} \quad (13)$$

$$\tau = 1 + 2 \sum_{k=1}^{\infty} \rho(k) \quad (14)$$

where N = number of the original samples; $\rho(k)$ = lag- k ACF of the autocorrelated time series; and τ = autocorrelation time. In our calculations, the infinite sum is truncated at the last lag- M where $\rho(M) + \rho(M+1) \geq 0$. Many statistical software packages also

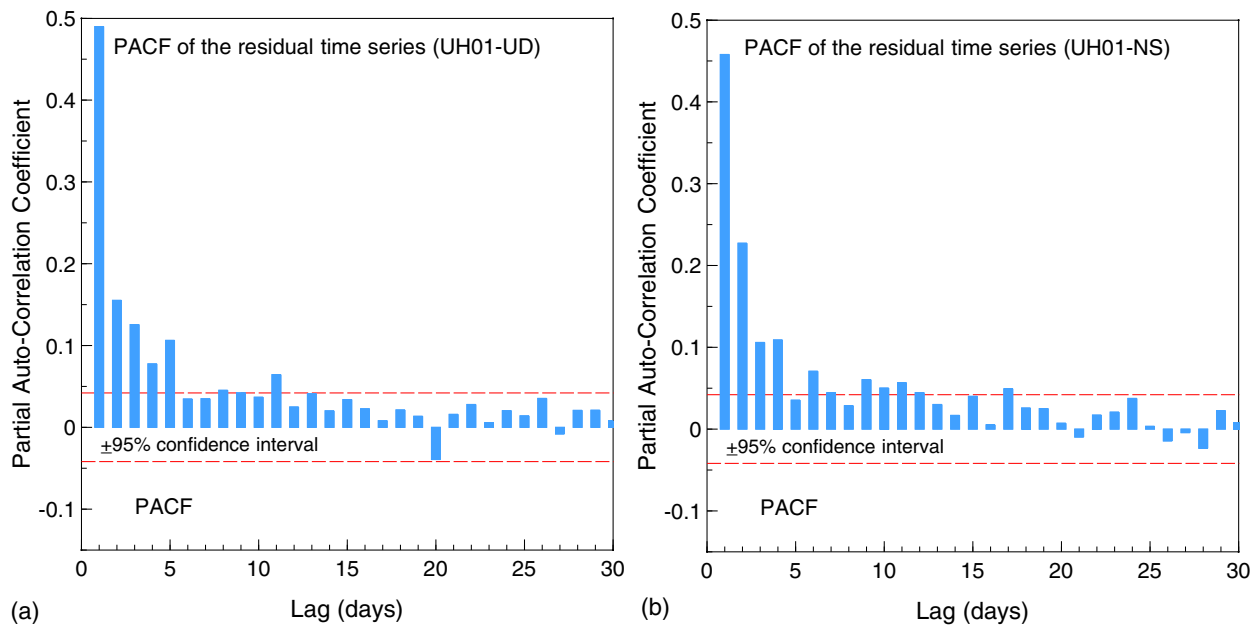


Fig. 5. PACF of the residual time series of the (a) vertical (up–down); and (b) horizontal (NS) components of UH01. The dashed lines represent the $\pm 95\%$ confidence interval of the PACF, estimated by $\pm 1.96/\sqrt{N}$, where N is the number of measurements.

adopt a similar approach. For example, the Stan statistical package, a state-of-the-art platform for statistical modeling and computation, cuts off the infinite sum at the first negative $\rho(k)$ (Stan Development Team 2021). The ACF in Fig. 4 suggests that the ACF after the lag- M is a zero-crossing undulating function of the time span. The parts below and above the x -axis retain approximately equal areas. Thus, $\sum_{k=M}^{\infty} \rho(k) \approx 0$. So, $\sum_{k=1}^M \rho(k)$ is a reasonable approximation of $\sum_{k=1}^{\infty} \rho(k)$. Accordingly, the corrected standard error [Eq. (8)] of the linear trend can be estimated by

$$\text{SE}_{bc} \approx \frac{s}{\sqrt{N_{\text{eff}}}} \times \frac{1}{\sigma_t} = \sqrt{\tau} \times \text{SE}_b \quad (15)$$

Assuming that the linear trends of the nonlinear and seasonal motions are flat (e.g., <0.1 mm/year), SE_{bc} would be a reasonable approximation of the uncertainty of the site velocity (b) from the ordinary regression. The 95%CI can be estimated by $1.96 \times \text{SE}_{bc}$. However, in many cases, the nonlinear motions show a remarkable linear trend drifting away from the zero velocity, which is mainly related to long-period (e.g., >1 year) motions or significantly non-stationary noises. The amplitudes of seasonal motions can be substantial in certain areas (up to a few centimeters), which could also result in a remarkable linear trend drifting away from the zero velocity if the time range is short (e.g., less than 3 years).

Fig. 6 illustrates a particular case (UTEX) in which the nonlinear motions and seasonal motions show remarkable linear trends (5 versus 8 years). UTEX lies in a subsiding area in western Houston. This region has been suffering from land subsidence associated with excessive groundwater withdrawals for more than five decades (e.g., Kearns et al. 2015; Liu et al. 2019). The ongoing average subsidence rate is approximately 9 mm/year (2012–2020) with respect to GOM20. The antenna is installed on the sidewall of a 2-story building [Fig. 2(c)]. The nonlinear motions result in a linear trend (b_{NL}) of 0.35 mm/year within the 5-year window (2012.4–2017.4) and an even larger linear trend (0.77 mm/year) within the 8-year window (2012.4–2020.4). The seasonal motions result in an overall linear trend (b_S) of 0.41 mm/year within the 5-year segment and a smaller linear trend (0.12 mm/year) within the

8-year window. The b_{NL} and b_S are the velocity errors from the deterministic part of the original GNSS time series [Eq. (9)]. Both degrade the confidence of the ordinary linear regression result (b) in almost a certain way (~100%). Accordingly, the 95%CI of the site velocity b could be estimated by $1.96 \times \text{SE}_{bc}$, plus the absolute values of the linear trends of the nonlinear and the seasonal motions

$$b_{95\%CI} \approx 1.96 \times \text{SE}_{bc} + |b_{NL}| + |b_S| \quad (16)$$

For stations located on stable sites (e.g., bedrock) or stations with a history of more than 5 years, b_{NL} and b_S are often ignorable (<0.2 mm/year). A statistical analysis of the contribution of b_{NL} and b_S to the 95%CI will be investigated in the next section. Throughout this article, the 95%CI is calculated according to Eq. (16).

Empirical Formulas for Projecting the 95%CI

In this section, I calculate the 95%CI of the site velocities at approximately 13,000 globally distributed GNSS stations with observations over 400 days. The daily PPP solutions (ECEF-XYZ, with respect to IGS14) are provided by NGL (Blewitt et al. 2018) and the Houston GPS Network (Wang et al. 2015b). The XYZ time series is converted to a local topocentric coordinate system, called local-ENU coordinates: EW, NS, and up–down (UD). An outlier-removing procedure introduced in Wang (2011, 2013) is employed to remove obvious outliers. On average, about 2% of measurements are removed as outliers. GNSS stations with less than 270 observational days per year (9 months per year) are excluded from the global data set. Site movements at some GNSS sites do not follow a linear relationship over time, such as sites significantly affected by long-term postseismic displacements, subsidence, volcanic activities, and glacial movements. Those stations need to be excluded from the data set for assessing the linear regression. I find that the RMS of the residuals [Eq. (6)] after removing the overall linear trend can be used as a threshold to exclude those nonlinear sites. According to previous publications (e.g., Bertiger et al. 2010, 2020;

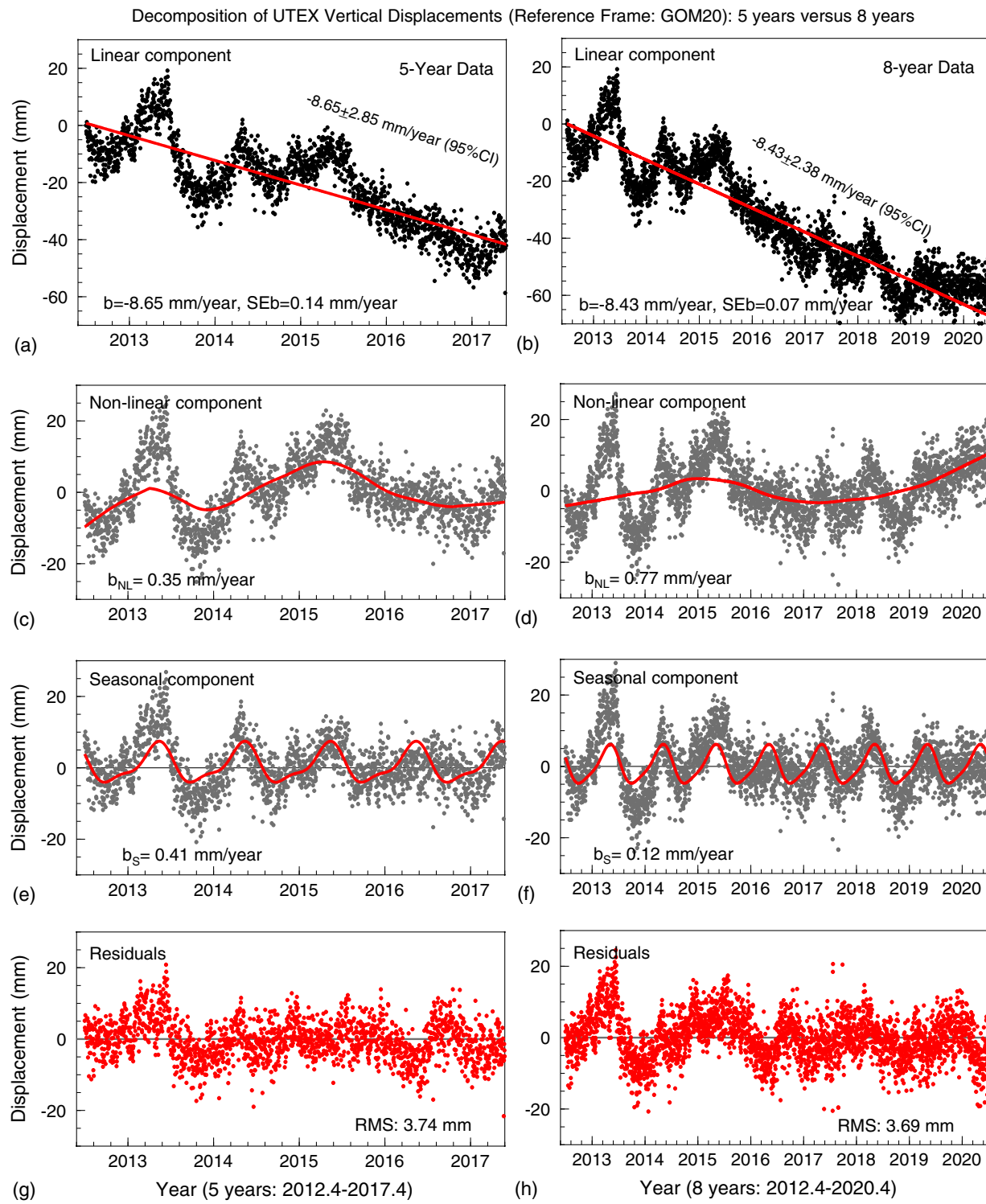


Fig. 6. Remarkable linear trends of the nonlinear motions and the seasonal motions at UTEX (vertical direction), 5 versus 8 years, respectively: (a and b) average site velocities and uncertainties (95%CI) corresponding to different year ranges; (c and d) linear trend (b_{NL}) of the nonlinear motions versus the year range; (e and f) linear trend (b_s) of the seasonal motions versus the year range; and (g and h) residual time series.

Wang et al. 2017) and this study, the average RMS of the daily PPP solutions for sites experiencing linear movements is below 4 mm for the horizontal components and below 8 mm for the vertical component. The time series at nonlinear sites often retain substantially larger RMS at least in one direction. I use RMS thresholds of 8 and 16 mm for the horizontal and vertical components, respectively, to exclude nonlinear sites. I checked many stations that were investigated in previous publications, such as GNSS sites significantly

affected by coseismic displacements and long-term postseismic deformation in China (Wang et al. 2018; Bao et al. 2021), sites with antennas covered by snow during the winter in Alaska (Wang et al. 2015a), sites affected by volcanic activities in the Caribbean (Wang et al. 2019), and sites affected by significant nonlinear subsidence in the greater Houston region (Agudelo et al. 2020). Those stations have been successfully rejected by the RMS thresholds. After all these selections, 9,700 displacement time series remained for the

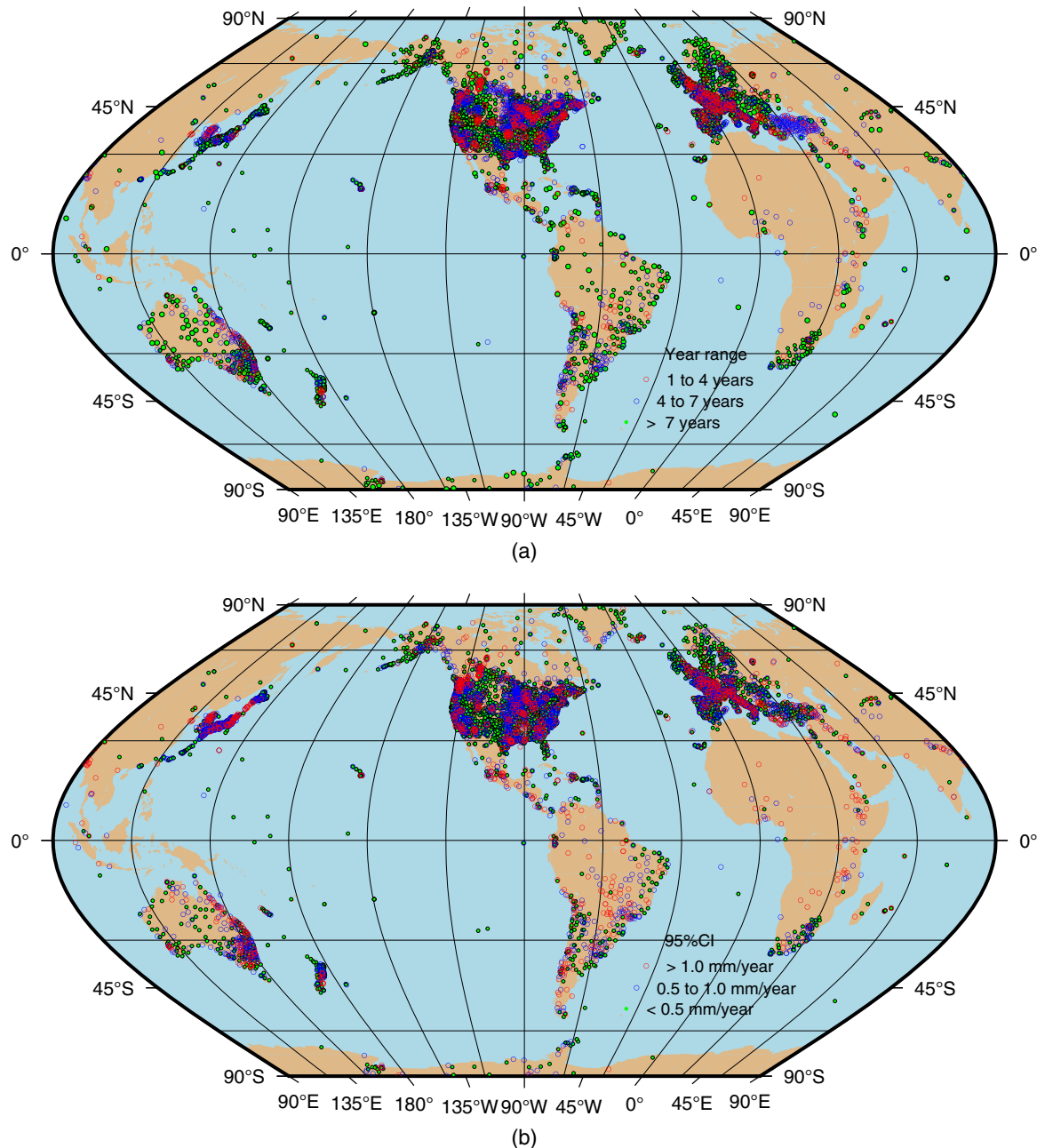


Fig. 7. Global distributions of the selected GNSS (approximately 9,700) for developing the empirical formula predicting the 95%CI of the vertical site velocities [Eq. (18)]: (a) observational periods; and (b) 95%CI.

vertical component, 9,700 for the NS component, and 9,600 for the EW component. The vertical and horizontal components are treated separately in this study. The remaining stations for the three components are slightly different.

Fig. 7 depicts the locations of those 9,700 GNSS stations whose vertical time series remained for the statistical analysis. The maps are plotted with the Generic Mapping Tools (GMT) (Wessel et al. 2013). The majority GNSS stations are in the US, Europe, and Japan. Fig. 7(a) depicts the observational history of these 9,700 stations; the colors represent the year range: over 7 years, between 4 and 7 years, and between 1 and 4 years. Fig. 7(b) depicts the 95% CI of the vertical velocities; the colors represent the levels of the 95%CI: below 0.5 mm/year, between 0.5 and 1.0 mm/year, and greater than 1.0 mm/year. The color patterns suggest that the 95% CI is primarily dominated by the time span of the observations.

Fig. 8 illustrates the 95%CI of the site velocities at these 9,700 GNSS stations versus the year range of the observations. The log-log plots indicate a linear relationship between $\log(95\% \text{CI})$ and $\log(T)$ for both vertical and horizontal components, suggesting a power-law relationship between the 95%CI and the year range. Each horizontal component can be best fit by a regression line

$$95\% \text{CI} = 1.8 \times \frac{1}{T} \quad (17)$$

The vertical component can be best fit by a regression line

$$95\% \text{CI} = 5.2 \times \frac{1}{T^{1.25}} \quad (18)$$

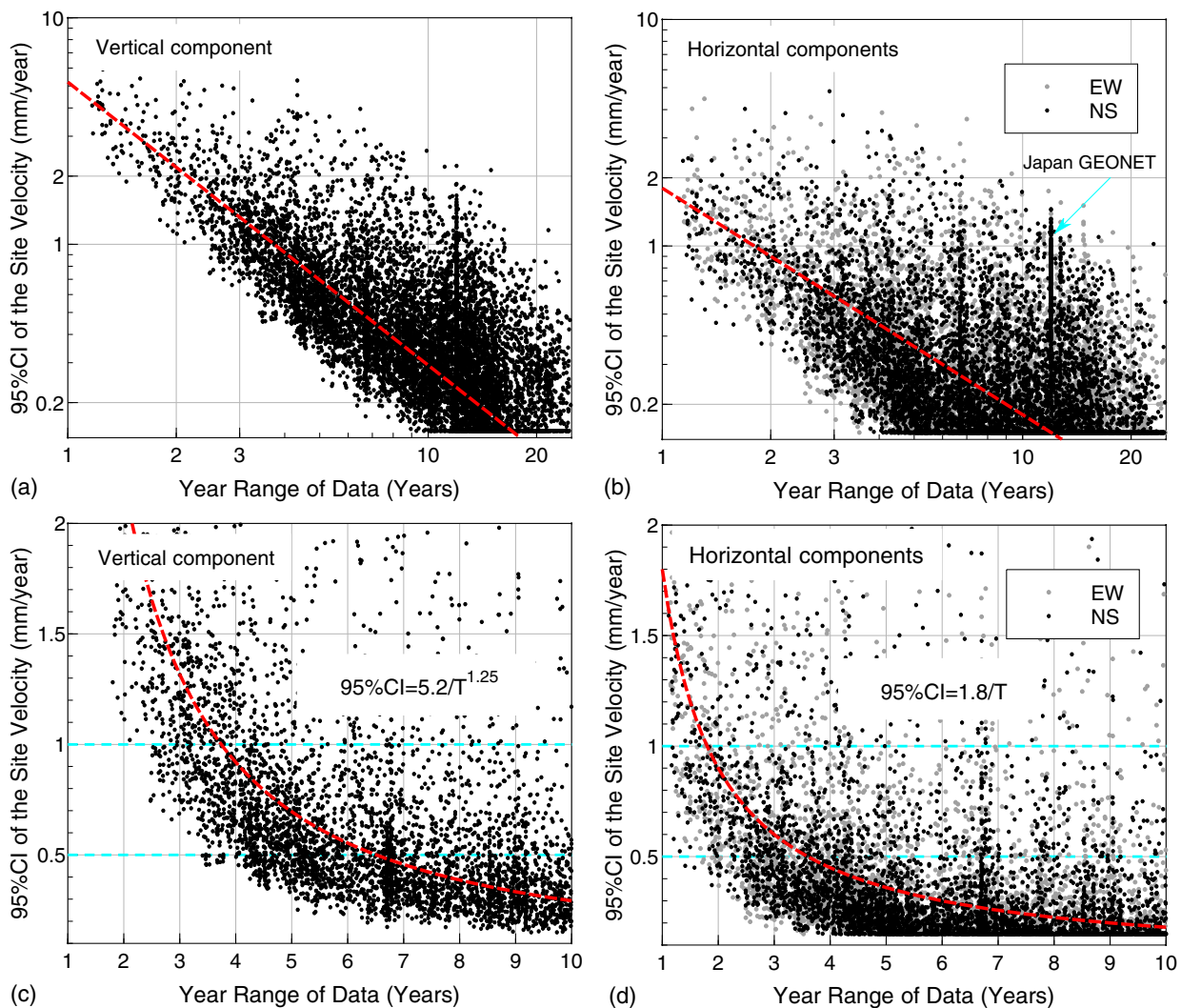


Fig. 8. 95%CI of site velocities versus the year range at 9,700 globally distributed GNSS stations: (a and b) log-log plots of the 95%CI versus the year range for the vertical and horizontal (EW, NS) components, respectively; and (c and d) linear plots within a smaller range for the vertical and horizontal (EW, NS) components, respectively. The locations of GNSS used for the vertical component are plotted in Fig. 7.

where T = year range of the time series in years; and the unit of 95% CI is in millimeters per year. The 95%CI tends to decrease rapidly with the increase of time span. The empirical formulas [Eqs. (17) and (18)] provide a general tool for users to project the ideal observational time span for their deformation monitoring projects. In order to achieve a 95%CI below 1 mm/year for a horizontal site velocity, continuous observations over 2.5 years are recommended. In order to achieve a 95%CI below 1 mm/year in all three directions, continuous GNSS observations over 4 years are needed. A minimum of 7 years of observations are recommended for achieving a 95%CI below 0.5 mm/year in all three directions.

Fig. 9 depicts the contributions of the nonlinear and seasonal motions to the 95%CI of site velocities [Eq. (16)]. Both the linear trends of the nonlinear and seasonal motions decay with the increase of the year range. The linear trend b_S of the seasonal motions shows regular undulations with a 1-year period [Figs. 9(a and b)]. The undulations reduce to below 0.2 mm/year approximately after 4.5 annual cycles in each horizontal direction and after 6.5 annual cycles in the vertical direction. However, the linear trend b_{NL} of the nonlinear motions is more site specific [Figs. 9(c and d)]. Figs. 9(a and b) also suggest that the velocity estimated from an $n - 0.5$ year time series may suffer less impact from seasonal motions than an

n year time series. In the geodesy research community, a minimum of a 2.5-year time span of coordinate time series is often recommended to minimize the effect of seasonal ground motions (e.g., Blewitt and Lavallee 2002). Fig. 9 indicates that the effect of vertical seasonal motions for time series over 2.5 years could still be remarkable (>0.2 mm/year). According to the empirical formulas [Eqs. (17) and (18)], the 95%CI of the site velocity for the 2.5-year time series is 0.7 mm/year in the horizontal direction and 1.7 mm/year in the vertical direction. For stability monitoring projects focusing on submillimeter-per-year accuracy (95%CI) in the vertical direction, observations longer than 4 years are needed.

Robustness and Limitations

Noise and data gaps are two key elements increasing the velocity uncertainty of the GNSS time series. A robust 95%CI estimator is expected to distinguish sites with significant noise and large gaps from average sites. It may be easier to describe what is not an average site than what is an average site. For example, those sites affected by irregular fluctuations of groundwater levels, short-period severe drought or flooding, snow or ice on antennas during the

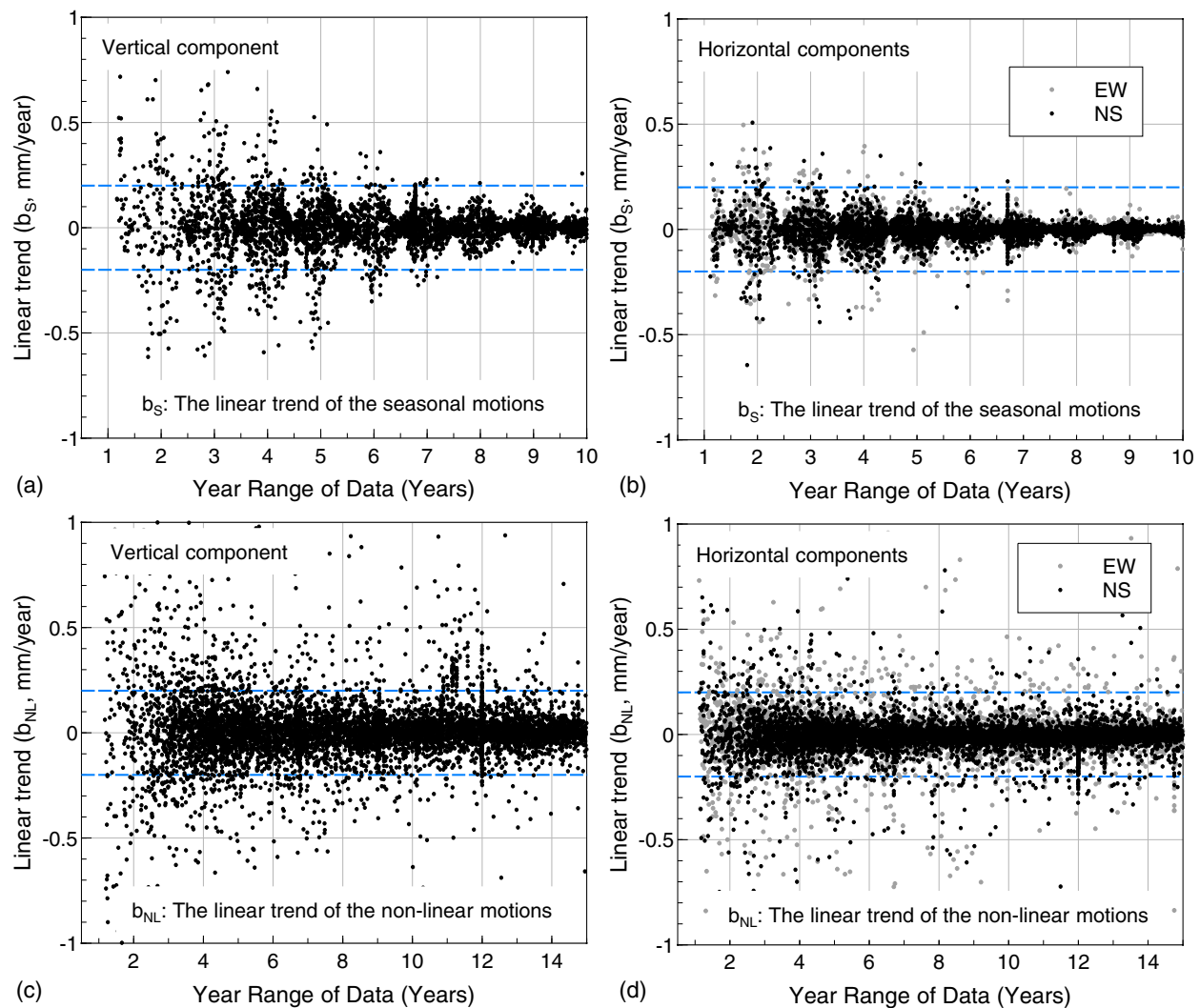


Fig. 9. (a and b) Linear trends (b_S) of the seasonal motions versus the year range at these 9,700 globally distributed GNSS sites for the vertical and horizontal components, respectively; and (c and d) linear trends (b_{NL}) of the nonlinear motions versus the year range at these 9,700 globally distributed GNSS sites for the vertical and horizontal components, respectively.

winter, localized landslide and fault creeping, and significant post-seismic displacements are not average sites.

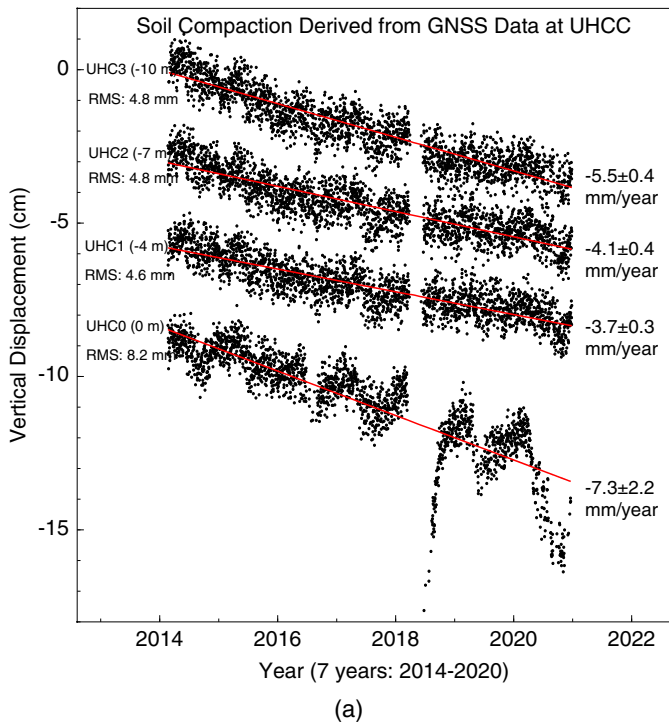
Effects of Site-Specific Noise

The scatterplots in Fig. 8 indicate that the 95%CI estimates are remarkably scattered around the regression line. Fig. 9 suggests that the scattering is partially contributed by b_{NL} , site-specific nonlinear motions. Fig. 10(a) illustrates the vertical displacement time series recorded by a GNSS array at the University of Houston Coastal Center (UHCC). The GPS array was designed to measure the sediment compactions at different depths. The antenna poles are anchored at the bottom of boreholes cased with PVC pipes. The depths of the boreholes at UHC3, UHC2, and UHC1 are 10, 7, and 4 m below the land surface, respectively [Fig. 10(b)]. The antennas move consistently with the vertical movements of the bottom sediments. The antenna pole of UHC0 is just anchored on a concrete pad built on the ground surface. The vertical component of UHC3, UHC2, and UHC1 recorded different compaction rates associated with the different thicknesses of sediments. Visually, the noise levels of the time series at these three sites are the same. The 95%CI estimates at these three sites are almost identical, 0.3 to

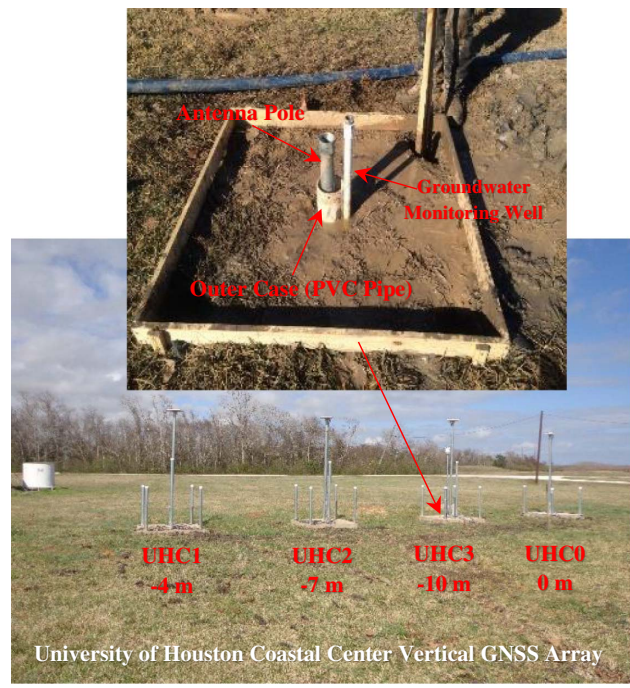
0.4 mm/year, comparable with the projections from Eq. (18) ($5.2 \times 7^{-1.25} = 0.46$ mm/year). The 95%CI at UHC0 is much larger than the 95%CI of deep-seated sites (0.4 versus 2.2 mm/year). The substantial noise at UHC0 is associated with land surface fluctuations caused by frequent soil moisture changes within the shallow soil. Fig. 10(a) suggests that the method [Eq. (16)] for calculating the 95%CI is robust in distinguishing noisy sites from normal sites. I further checked many other sites showing remarkable (>2 mm/year) 95%CI values. It is found that estimated site velocities at those sites are often biased by significant pulse-like motions or long-period (>1 year) motions superimposed into the time series. The observations at UHCC suggest that the 95%CI can be potentially used as an index for automatically sorting well-behaved and poorly behaved GNSS time series from GNSS networks with a similar observational time span.

Effects of Data Gaps

Missing data can create problems for analyzing time series. A common technique for handling missing data is imputation, whereby the missing data are filled in to create a continuous time series. The methods for calculating ACF and PACF require



(a)



(b)

Fig. 10. Effects of the site noise on the 95%CI: (a) GNSS-derived subsidence time series at four closely spaced sites at UHCC; and (b) UHCC vertical GNSS array.

continuous time series. The decomposition process also requires continuous time series because FFT is involved in the seasonality analysis [Eq. (10)]. So, all gaps need to be filled before calculating the 95%CI. Scientists have embraced many theories and methods to fill missing data. In general, those methods work well for small gaps (a few days) and poorly for large gaps (a few months to years). The hot-deck imputation method is employed for filling missing data in this study.

Fig. 11 depicts the comparison of original and gap-filled displacement time series (vertical) at TXWO and PA26. TXWO is a typical continuously operating reference station (CORS) operated by the Texas Department of Transportation. TXWO is located in the City of Woodville, Tyler County, Texas. There are several small gaps (a few days) and one large gap (approximately half a year) in the observations at TXWO. The average data rate is 310 days per year. Visually, the imputation does a good job filling small gaps. The calculated 95%CI is 0.77 mm/year for TXWO, which is slightly larger than the projection from Eq. (18) (0.70 mm/year). PA26 was a periodically surveyed GNSS station operated by the Houston–Galveston Subsidence District in Houston. PA26 was switched to a continuous GNSS station in 2017. There are frequent gaps from a few days to a few months within the original time series. The average data rate is 265 days per year. The calculated 95%CI is 1.46 mm/year, which is about two times the projection [Eq. (18), 0.70 mm/year]. PA26 retains more gaps than the sites (a minimum of 270 days per year) used to establish the regression model [Eq. (18)]. So, the larger 95%CI at PA26 is expected. It is evident that the method for calculating the 95%CI is able to account for the effect of data gaps on the velocity uncertainties.

Limitations

The general methodology for calculating the 95%CI [Eq. (16)] is applicable to GNSS time series at any sites processed with different methods. The empirical formulas [Eqs. (17) and (18)] for projecting

95%CI are derived from the daily positional time series processed by the GipsyX software package (Bertiger et al. 2020). GipsyX achieves higher accuracy than its predecessor GIPSY-OASIS (Bertiger et al. 2010), and it is constantly updated and upgraded. In general, a new software package or a new version often achieves higher accuracy than its predecessors because the new version always tries to integrate the latest models and data processing techniques. As a result, the uncertainty from recently processed positional time series may be considerably smaller than those published uncertainties a few years ago. Different GNSS data processing methods often produce positional time series with slightly different scatters (Wang et al. 2017). Thus, the uncertainties of the velocity products from different research groups (often using different software packages and parameters) could be considerably different. The definition of the 95%CI introduced in this study [Eq. (16)] may differ from the definition of the uncertainties used in other publications. For the reasons mentioned previously, I do not recommend mixing the velocity uncertainties determined from the method introduced in this study with the uncertainties determined with other methods or provided by other research groups.

This study further indicates that the uncertainty could be highly site specific (e.g., Figs. 8 and 10). It is likely that the empirical formulas [Eqs. (17) and (18)] developed in this study represent the optimistic projection of the 95%CI of GNSS site velocities because the time series used for this study are produced from the state-of-the-art (as of 2020) GNSS positioning techniques. Users may bear this in mind if they do need to compare the projected uncertainties from the empirical models [Eqs. (17) and (18)] with the published uncertainties in the geodesy literature.

The effects of data gaps on the 95%CI have not been fully investigated in this study. The hot-deck method does not rely on synthetic models fitting for the variable to be imputed, and thus is potentially less sensitive to model misspecifications than regression imputation methods. However, the hot-deck imputation employed in this study could introduce hidden variability because random

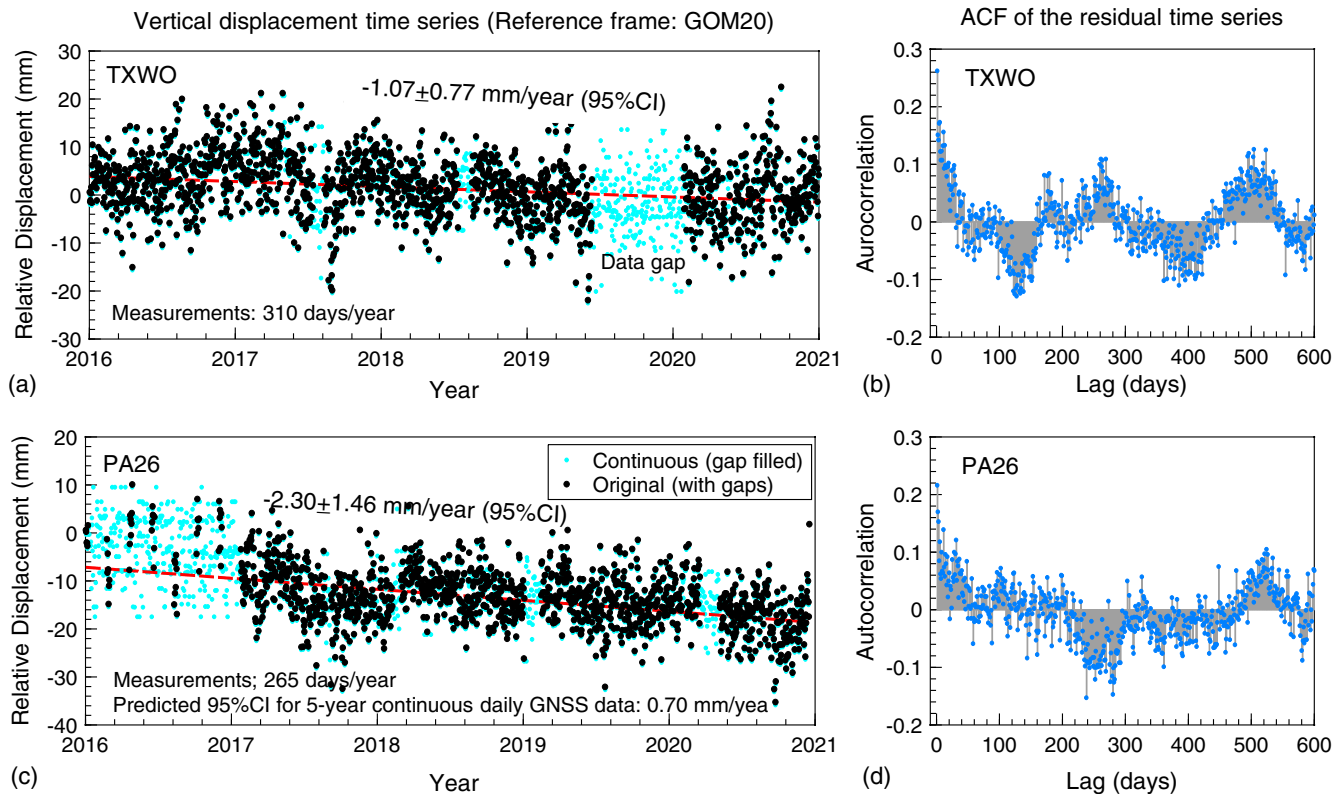


Fig. 11. Effects of data gaps on the 95%CI: (a) original and gap-filled displacement time series (vertical) at TXWO; (b) ACF of the residual time series (vertical) at TXWO; (c) original and gap-filled displacement time series (vertical) at PA26; and (d) ACF of the residual time series (vertical) at PA26.

weights are involved in filling data gaps. It thus breaks the temporal correlations within the original data, which may affect the estimates of ACF, and in turn affect the estimates of autocorrelation time (τ) and the 95%CI. In general, small gaps cause fewer impacts on the 95%CI than large gaps. The 95%CI from GNSS time series with large gaps from several months to a year should be interpreted with caution.

Determining the 95%CI of the Absolute Sea-Level Trend

Sea-level changes are primarily measured using TGs along the coasts. Instead of measuring absolute (eustatic) sea-level changes, TG measures sea-level changes with respect to adjacent benchmarks fixed on the local land surface. Therefore, the mean sea-level

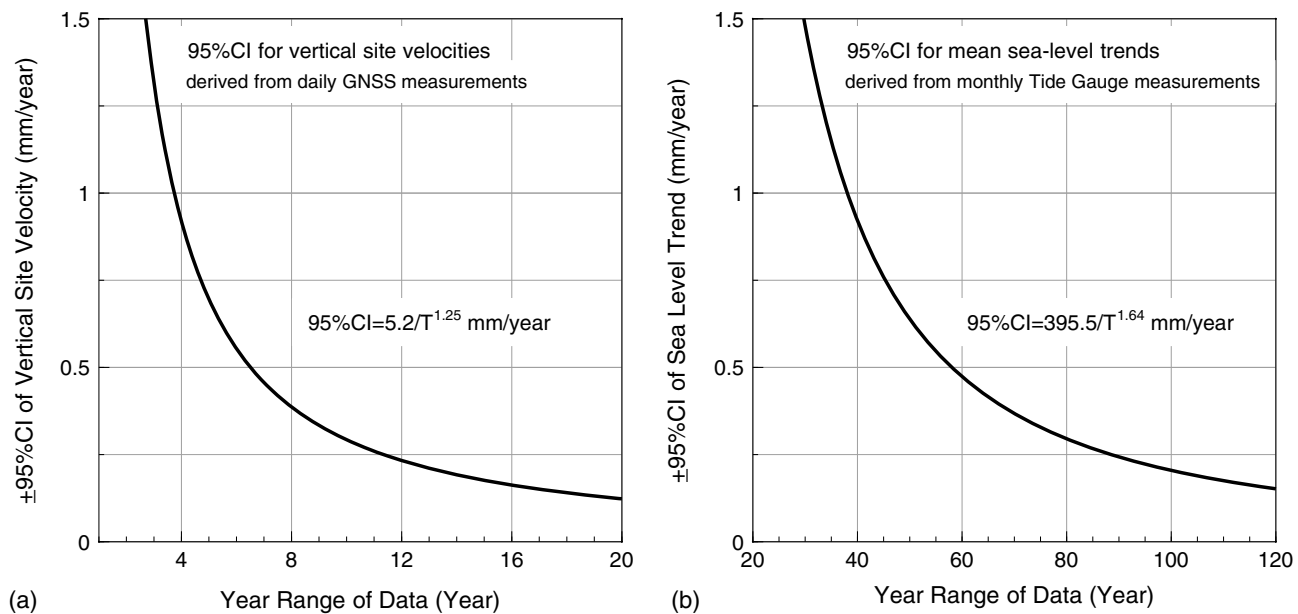


Fig. 12. (a) Projection model for 95%CI of the VLM rates versus the year range of the GNSS data [Eq. (18)]; and (b) projection model for the 95%CI of MSL rates versus the year range of the TG data [Eq. (20)].

(MSL) change rate derived from TG data (V_{TG}) is a combination of the absolute sea-level change rate (V_{ASL}) and the vertical land movement measured by GNSS (subsidence or uplift) rate (V_{GNSS}). The absolute sea-level change rate with respect to a global or regional reference frame can be estimated by

$$V_{ASL} = V_{TG} + V_{GNSS} \quad (19)$$

One challenge of using the closely spaced GNSS and TG data sets to estimate V_{ASL} is the mismatching of the uncertainties of V_{TG} and V_{GNSS} . To the best of my knowledge, there was not a consistent method for determining the uncertainties of V_{TG} and V_{GNSS} before this study. Thus, it is often confusing or troublesome for sea-level researchers and practical users to assess the uncertainties of the absolute sea-level trends (V_{ASL}).

The method for determining the 95%CI of the VLM rates introduced in this article is similar to the NOAA's method for determining the 95%CI of sea-level trends. Both methods employ an autoregressive model for accounting for the time-correlated noise within the observations. Researchers at NOAA developed the following empirical formula for projecting the 95%CI of the sea-level trends (Zervas 2009):

$$95\%CI = 395.5 \times \frac{1}{T^{1.64}} \quad (20)$$

where T = year range of the monthly sea-level measurements in years; and 95%CI is in millimeters per year. Fig. 12 illustrates

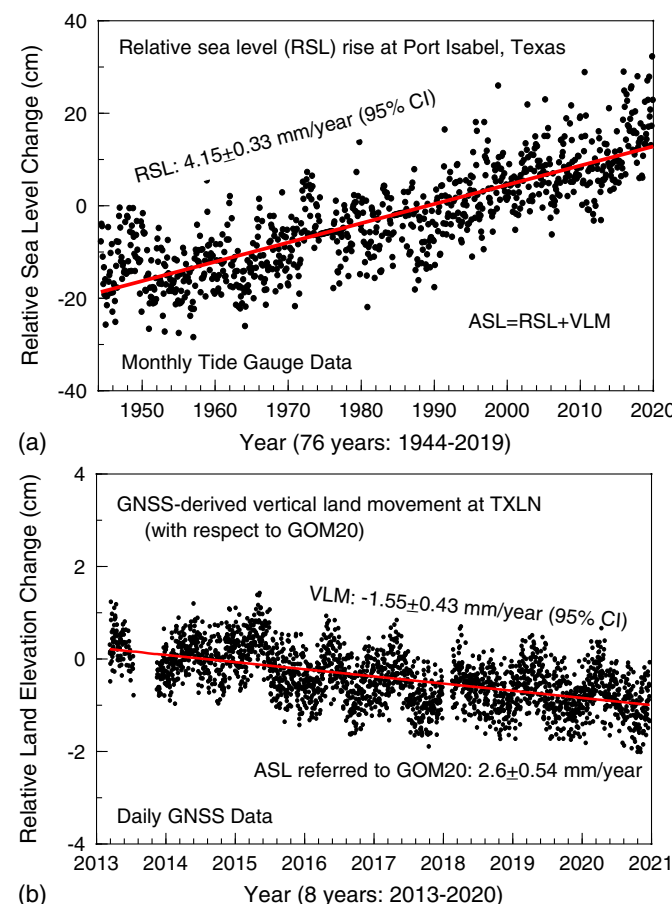


Fig. 13. (a) Relative sea-level (RSL) trend and 95%CI derived from 76-year monthly TG data at Port Isabel, Texas; and (b) VLM rate and 95%CI derived from 8-year daily GNSS data at TXLN.

the empirical models for predicting the 95%CI of GNSS-derived site velocities (vertical) and TG-derived sea-level trends [Eqs. (18) and (20)]. The plots suggest that approximately 4-year daily GNSS observations (vertical) and 40-year monthly TG observations are needed to achieve a 1-mm-per-year 95%CI. Many research scientists recommend using a minimum of 60 years of TG data for estimating global sea-level trends (e.g., IPCC 2013; Parker 2014; Wenzel and Schroter 2014). Seven-year daily GNSS observations would achieve the same 95%CI (~0.5 mm/year) as the 60-year monthly TG observations.

Fig. 13 illustrates a pair of the closely spaced TG and GNSS data sets at Port Isabel, Texas, near the Mexico and Texas border. TXLN is a CORS operated by the Texas Department of Transportation. The GNSS antenna is mounted on the sidewall of a single-story building [Fig. 2(d)]. The distance between the tide gauge and GNSS is about 9 km. The monthly sea-level measurements are provided by the Center for Operational Oceanographic Products and Services at NOAA. The 8-year GNSS measurements (2013–2020) result in an average land-subsidence rate of -1.55 mm/year with a 95%CI of 0.43 mm/year, which is slightly larger than the estimate from Eq. (18), 0.39 mm/year. The reference frame for the vertical land movements is GOM20, which provides a robust reference for ruling out regional tectonic movements and highlighting localized subsidence and faulting along the GOM coastal region. The 76-year monthly TG measurements (1944–2019) result in an average sea-level rise rate of 4.15 mm/year with a 95%CI of 0.33 mm/year [projection from Eq. (20): 0.33 mm/year]. The two rates result in an ongoing sea-level rise rate of 2.6 mm/year with respect to GOM20. According to the 95%CI estimates of V_{TG} and V_{GNSS} , the 95%CI of the sea-level rise rate (V_{ASL}) with respect to GOM20 would approximate to 0.5 mm/year ($\sqrt{0.33^2 + 0.43^2} = 0.54$).

Conclusions

This study presented a general methodology for determining the 95%CI [Eq. (16)] of the site velocities derived from GNSS daily positions affected by time-correlated noises. An effective sample size (N_{eff}) was used to calculate the standard error of the linear trend instead of the original sample size. The N_{eff} was obtained from a high-order autoregressive model of the residual time series. It was found that the 95%CI fits an inverse power-law relationship with the time span (T) of the GNSS observations. Two empirical formulas [Eqs. (17) and (18)] for projecting the 95%CI of horizontal and vertical site velocities were developed based on the data sets from approximately 9,700 globally distributed GNSS stations. The empirical formulas provide the projections for the 95%CI of site velocities processed with state-of-the-art GNSS techniques.

According to this study, a minimum of 2.5- and 4-year continuous GNSS observations are recommended to achieve a 95%CI at 1 mm/year for the horizontal and vertical site velocities, respectively; 4- and 7-year GNSS observations are recommended to achieve a 95%CI below 0.5 mm/year for the horizontal and vertical site velocities, respectively. Seven-year daily GNSS measurements would achieve a similar 95%CI (~0.5 mm/year) with the 60-year monthly tide gauge measurements, and 15-year GNSS data would achieve a similar 95%CI (~0.25 mm/year) with the 100-year tide gauge data. This study recommends that a 7-year period be adopted as a minimum time span of GNSS observations for sea-level rise and coastal submergence studies using closely spaced GNSS and TG data sets.

The 95%CI could potentially be a robust index for automatically sorting well-behaved and poorly behaved GNSS data sets from large GNSS networks with similar observational periods.

Considering the wide applications of the linear trends of GNSS time series in science and engineering, the methodology and the models introduced in this study have the potential for broad applications in geosciences, civil and surveying engineering, and sea-level rise and coastal submergence studies.

Data Availability Statement

All processed data, models, or code that support the findings of this study are available from the author upon request.

Acknowledgments

I acknowledge Geoff Blewitt and his team at the Nevada Geodetic Laboratory for sharing processed daily PPP solutions and colleagues at NOAA for sharing tide gauge data. I appreciate the thoughtful comments from the three reviewers.

References

- Agnew, D. C. 1992. "The time-domain behavior of power law noises." *Geophys. Res. Lett.* 19 (4): 333–336. <https://doi.org/10.1029/91GL02832>.
- Agudelo, G., G. Wang, Y. Liu, Y. Bao, and M. J. Turco. 2020. "GPS geodetic infrastructure for subsidence and fault monitoring in Houston, Texas, USA." *Proc. Int. Assoc. Hydrol. Sci.* 382 (Apr): 11–18. <https://doi.org/10.5194/piahs-97-1-2020>.
- Altamimi, Z., P. Rebischung, L. Métivier, and X. Collilieux. 2016. "ITRF2014: A new release of the International Terrestrial Reference Frame modeling nonlinear station motions." *J. Geophys. Res.* 121 (8): 6109–6131. <https://doi.org/10.1002/2016JB013098>.
- Bao, Y., W. Guo, G. Wang, W. Gan, M. Zhang, and J. S. Shen. 2018. "Millimeter-accuracy structural deformation monitoring using stand-alone GPS: Case study in Beijing, China." *J. Surv. Eng.* 144 (1): 05017007. [https://doi.org/10.1061/\(ASCE\)SU.1943-5428.0000242](https://doi.org/10.1061/(ASCE)SU.1943-5428.0000242).
- Bao, Y., X. Yu, G. Wang, H. Zhou, X. Ding, G. Xiao, S. Shen, R. Zhao, and W. Gan. 2021. "SChina20: A stable geodetic reference frame for ground movement and structural deformation monitoring in South China." *J. Surv. Eng.* 147 (3): 04021006. [https://doi.org/10.1061/\(ASCE\)SU.1943-5428.0000352](https://doi.org/10.1061/(ASCE)SU.1943-5428.0000352).
- Bertiger, W., et al. 2020. "GipsyX/RTGx, a new tool set for space geodetic operations and research." *Adv. Space Res.* 66 (3): 469–489. <https://doi.org/10.1016/j.asr.2020.04.015>.
- Bertiger, W., S. D. Desai, B. Haines, N. Harvey, A. W. Moore, S. Owen, and J. P. Weiss. 2010. "Single receiver phase ambiguity resolution with GPS data." *J. Geod.* 84 (5): 327–337. <https://doi.org/10.1007/s00190-010-0371-9>.
- Bettinelli, P., J. P. Avouac, M. Flouzat, F. Jouanne, L. Bollinger, P. Willis, and G. R. Chitrakar. 2006. "Plate motion of India and interseismic strain in the Nepal Himalaya from GPS and DORIS measurements." *J. Geod.* 80 (8): 567–589. <https://doi.org/10.1007/s00190-006-0030-3>.
- Blewitt, G., W. C. Hammond, and C. Kreemer. 2018. "Harnessing the GPS data explosion for interdisciplinary science." *Eos* 99 (10.1029): 485. <https://doi.org/10.1029/2018EO104623>.
- Blewitt, G., C. Kreemer, W. C. Hammond, and J. Gazeaux. 2016. "MIDAS robust trend estimator for accurate GPS station velocities without step detection." *J. Geophys. Res.* 121 (3): 2054–2068. <https://doi.org/10.1002/2015JB012552>.
- Blewitt, G., and D. Lavallee. 2002. "Effect of annual signals on geodetic velocity." *J. Geophys. Res.* 107 (B7): ETG-9. <https://doi.org/10.1029/2001JB000570>.
- Bogusz, J. 2015. "Geodetic aspects of GPS permanent stations non-linearity studies." *Acta Geodyn. Geomater.* 12 (4): 323–333. <https://doi.org/10.13168/AGG.2015.0033>.
- Bos, M. S., R. M. S. Fernandes, S. D. P. Williams, and L. Bastos. 2013. "Fast error analysis of continuous GNSS observations with missing data." *J. Geod.* 87 (4): 351–360. <https://doi.org/10.1007/s00190-012-0605-0>.
- Box, G. E. P., G. M. Jenkins, and G. C. Reinsel. 2008. *Time series analysis, forecasting and control*. 4th ed. Hoboken, NJ: Wiley.
- Chen, Q., T. van Dan, N. Sneeuw, X. Collilieux, M. Weigelt, and P. Rebischung. 2013. "Singular spectrum analysis for modeling seasonal signals from GPS time series." *J. Geodyn.* 72 (2013): 25–35. <https://doi.org/10.1016/j.jog.2013.05.005>.
- Cleveland, W. S. 1981. "LOWESS: A program for smoothing scatterplots by robust locally weighted regression." *Am. Stat.* 35 (1): 54. <https://doi.org/10.2307/2683591>.
- Davis, J. L., B. P. Wernicke, and M. E. Tamisiea. 2012. "On seasonal signals in geodetic time series." *J. Geophys. Res.* 117 (B1): B01403. <https://doi.org/10.1029/2011JB008690>.
- Didova, O., B. Gunter, R. Riva, R. Klees, and L. Roese-Koerner. 2016. "An approach for estimating time-variable rates from geodetic time series." *J. Geod.* 90 (11): 1207–1221. <https://doi.org/10.1007/s00190-016-0918-5>.
- Dixon, T. H., M. Killer, F. Farina, H. Wang, and D. Wang. 2000. "Present-day motion of the Sierra Nevada block and some tectonic implications for the Basin and Range province, North American Cordillera." *Tectonics* 19 (1): 1–24. <https://doi.org/10.1029/1998TC001088>.
- Dong, D., P. Fang, Y. Bock, M. K. Cheng, and S. Miyazaki. 2002. "Anatomy of apparent seasonal variations from GPS-derived site position time series." *J. Geophys. Res.* 107 (B4): 2075. <https://doi.org/10.1029/2001JB000573>.
- Ford, B. L. 1983. "An overview of hot-deck procedures." In Vol. 2 of *Incomplete data in sample surveys*, edited by W. G. Madow, I. Olkin, and D. B. Rubin, 185–207. New York: Academic.
- Geyer, C. J. 1992. "Practical Markov chain Monte Carlo." *Stat. Sci.* 7 (4): 473–483. <https://doi.org/10.1214/ss/1177011137>.
- Griffiths, J., and J. Ray. 2009. "On the precision and accuracy of IGS orbits." *J. Geod.* 83 (3): 277–287. <https://doi.org/10.1007/s00190-008-0237-6>.
- Guo, W., G. Wang, Y. Bao, P. Li, M. Zhang, Q. Gong, R. Li, Y. Gao, R. Zhao, and S. Shen. 2019. "Detection and monitoring of tunneling-induced riverbed deformation using GPS and BeiDou: A case study." *Appl. Sci.* 9 (13): 2759. <https://doi.org/10.3390/app9132759>.
- Hackl, M., R. Malservisi, U. Hugentobler, and R. Wonnacott. 2011. "Estimation of velocity uncertainties from GPS time series: Examples from the analysis of the South African TrigNet network." *J. Geophys. Res.* 116 (B11): 11404. <https://doi.org/10.1029/2010JB008142>.
- Heflin, M., A. Donnellan, J. Parker, G. Lyzenga, A. Moore, L. G. Ludwig, J. Rundle, J. Wang, and M. Pierce. 2020. "Automated estimation and tools to extract positions, velocities, breaks, and seasonal terms from daily GNSS measurements: Illuminating nonlinear Salton Trough deformation." *Earth Space Sci.* 7 (7): e2019EA000644. <https://doi.org/10.1029/2019EA000644>.
- Herring, T. A., T. I. Melbourne, M. H. Murray, M. A. Floyd, W. M. Szeliga, R. W. King, D. A. Phillips, C. M. Puskas, M. Santillan, and L. Wang. 2016. "Plate boundary observatory and related networks: GPS data analysis methods and geodetic products." *Rev. Geophys.* 54 (4): 759–808. <https://doi.org/10.1002/2016RG000529>.
- IPCC (Intergovernmental Panel on Climate Change). 2013. *Climate change 2013: The physical science basis. Contribution of Working Group I to the Fifth Assessment Report of the Intergovernmental Panel on Climate Change*. Edited by T. F. Stocker, D. Qin, G. K. Plattner, M. Tignor, S. K. Allen, J. Boschung, A. Nauels, Y. Xia, V. Bex, and P. M. Midgley. Cambridge, UK: Cambridge University Press. <https://doi.org/10.1017/CBO9781107415324>.
- JPL (Jet Propulsion Laboratory). 2021. "Time series for THSU." Accessed January 20, 2021. <https://sideshow.jpl.nasa.gov/post/links/THSU.html>.
- Kass, R. E., B. P. Carlin, A. Gelman, and R. Neal. 1998. "Markov chain Monte Carlo in practice: A roundtable discussion." *Am. Stat.* 52 (2): 93–100. <https://doi.org/10.2307/2685466>.
- Kearns, T. J., G. Wang, Y. Bao, J. Jiang, and D. Lee. 2015. "Current land subsidence and groundwater level changes in the Houston metropolitan area (2005–2012)." *J. Surv. Eng.* 141 (4): 05015002. [https://doi.org/10.1061/\(ASCE\)SU.1943-5428.0000147](https://doi.org/10.1061/(ASCE)SU.1943-5428.0000147).

- King, M. A., and S. D. P. Williams. 2009. "Apparent stability of GPS monumentation from short-baseline time series." *J. Geophys. Res.* 114 (B10): B10403. <https://doi.org/10.1029/2009JB006319>.
- Klos, A., J. Bogusz, M. Figurski, and W. Kosek. 2014. "Uncertainties of geodetic velocities from permanent GPS observations: The Sudeten case study." *Acta Geodyn. Geomater.* 11 (3): 201–209. <https://doi.org/10.13168/AGG.2014.0005>.
- Klos, A., M. S. Bos, and J. Bogusz. 2018. "Detecting time-varying seasonal signal in GPS position time series with different noise levels." *GPS Solut.* 22: 21. <https://doi.org/10.1007/s10291-017-0686-6>.
- Krarup, T. 1969. "A contribution to the mathematical foundation of physical geodesy." *Geod. Inst. Med.* 44: 80.
- Langbein, J. 2004. "In two-color electronic distance meter measurements revisited." *J. Geophys. Res.* 109 (B4): B04406. <https://doi.org/10.1029/2003JB002819>.
- Langbein, J. 2008. "Noise in GPS displacement measurements from Southern California and Southern Nevada." *J. Geophys. Res.* 113 (B5): B05405. <https://doi.org/10.1029/2007JB005247>.
- Langbein, J. 2012. "Estimating rate uncertainty with maximum likelihood: Differences between power-law and flicker-random-walk models." *J. Geod.* 86 (9): 775–783. <https://doi.org/10.1007/s00190-012-0556-5>.
- Langbein, J. 2017. "Improved efficiency of maximum likelihood analysis of time series with temporally correlated errors." *J. Geod.* 91: 985–994. <https://doi.org/10.1007/s00190-017-1002-5>.
- Langbein, J., and H. Johnson. 1997. "Correlated errors in geodetic time series: Implication for time dependent deformations." *J. Geophys. Res.* 102 (B1): 591–603. <https://doi.org/10.1029/96JB02945>.
- Liu, Y., X. Sun, G. Wang, M. J. Turco, G. Agudelo, Y. Bao, R. Zhao, and S. Shen. 2019. "Current activity of the long point fault in Houston, Texas constrained by continuous GPS measurements (2013–2018)." *Remote Sens.* 11 (10): 1213. <https://doi.org/10.3390/rs11101213>.
- Mao, A., C. A. Harrison, and T. H. Dixon. 1999. "Noise in GPS coordinate time series." *J. Geophys. Res.* 104 (B2): 2797–2816. <https://doi.org/10.1029/1998JB900033>.
- Moritz, H. 1973. "Least-squares collocation." *Publ. Deut. Geod. Komm.* A 75: 91.
- Murray, J. R., and J. Svarc. 2017. "Global positioning system data collection, processing, and analysis conducted by the US Geological Survey Earthquake Hazards Program." *Seismol. Res. Lett.* 88 (3): 916–925. <https://doi.org/10.1785/0220160204>.
- NGL (Nevada Geodetic Laboratory). 2021. "Station ID: THSU continuously updated data set." Accessed January 20, 2021. <http://geodesy.unr.edu/NGLStationPages/stations/THSU.sta>.
- Parker, A. 2014. "Minimum 60 years of recording are needed to compute the sea level rate of rise in the Western South Pacific." *Nonlinear Eng.* 3 (1): 1–10. <https://doi.org/10.1515/nleng-2013-0011>.
- Ray, J. M., M. S. Vijayan, and A. Kumar. 2019. "Noise characteristics of GPS time series and their influence on velocity uncertainties." *J. Earth Syst. Sci.* 128 (6): 146. <https://doi.org/10.1007/s12040-019-1179-5>.
- Rebisching, P., Z. Altamimi, J. Ray, and B. Garay. 2016. "The IGS contribution to ITRF2014." *J. Geod.* 90 (7): 611–630. <https://doi.org/10.1007/s00190-016-0897-6>.
- Santamaría-Gómez, A., M. Gravelle, X. Collilieux, M. Guichard, B. M. Miguez, P. Tiphaneau, and G. Wöppelmann. 2012. "Mitigating the effects of vertical land motion in tide gauge records using a state-of-the-art GPS velocity field." *Global Planet. Change* 98–99 (Dec): 6–17. <https://doi.org/10.1016/j.gloplacha.2012.07.007>.
- Snay, R., M. Cline, W. Dillinger, R. Foote, S. Hilla, W. Kass, J. Ray, J. Rohde, G. Sella, and T. Soler. 2007. "Using global positioning system-derived crustal velocities to estimate rates of absolute sea level change from North American tide gauge records." *J. Geophys. Res.* 112 (B4): B04409. <https://doi.org/10.1029/2006JB004606>.
- Soler, T., and G. Wang. 2016. "Interpreting OPUS-Static results accurately." *J. Surv. Eng.* 142 (4): 05016003. [https://doi.org/10.1061/\(ASCE\)SU.1943-5428.0000191](https://doi.org/10.1061/(ASCE)SU.1943-5428.0000191).
- Stan Development Team. 2021. "Stan user's guide, version 2.28." Accessed November 1, 2021. https://mc-stan.org/docs/2_28/stan-users-guide/index.html.
- Straatsma, T. P., H. J. C. Berendsen, and A. J. Stam. 1986. "Estimation of statistical errors in molecular simulation calculations." *Mol. Phys.* 57 (1): 89–95. <https://doi.org/10.1080/00268978600100071>.
- Thompson, M. B. 2010. *A comparison of methods for computing autocorrelation time*. Technical Rep. No. 1007. Toronto: Univ. of Toronto.
- Wang, G. 2011. "GPS landslide monitoring: Single base vs. network solutions, a case study based on the Puerto Rico and Virgin Islands permanent GPS network." *J. Geodetic Sci.* 1 (3): 191–203. <https://doi.org/10.2478/v10156-010-0022-3>.
- Wang, G. 2013. "Millimeter-accuracy GPS landslide monitoring using precise point positioning with single receiver phase ambiguity resolution: A case study in Puerto Rico." *J. Geodetic Sci.* 3 (1): 22–31. <https://doi.org/10.2478/jogs-2013-0001>.
- Wang, G., Y. Bao, Y. Cuddus, X. Jia, J. Serna, and Q. Jing. 2015a. "A methodology to derive precise landslide displacements from GPS observations in tectonically active and cold regions: A case study in Alaska." *Nat. Hazards* 77 (3): 1939–1961. <https://doi.org/10.1007/s11069-015-1684-z>.
- Wang, G., Y. Bao, W. Gan, J. Geng, G. Xiao, and J. S. Shen. 2018. "NChina16, a stable geodetic reference frame for geological hazard studies in North China." *J. Geodyn.* 115 (Apr): 10–22. <https://doi.org/10.1016/j.jog.2018.01.003>.
- Wang, G., T. J. Kearns, J. Yu, and G. Saenz. 2014. "A stable reference frame for landslide monitoring using GPS in the Puerto Rico and Virgin Islands Region." *Landslides* 11 (1): 119–129. <https://doi.org/10.1007/s10346-013-0428-y>.
- Wang, G., H. Liu, G. S. Mattioli, M. M. Miller, K. Feaux, and J. Braun. 2019. "CARIB18, a stable geodetic reference frame for geological hazard monitoring in the Caribbean region." *Remote Sens.* 11 (6): 680. <https://doi.org/10.3390/rs11060680>.
- Wang, G., M. J. Turco, T. Soler, T. J. Kearns, and J. Welch. 2017. "Comparisons of OPUS and PPP solutions for subsidence monitoring in the greater Houston area." *J. Surv. Eng.* 143 (4): 05017005. [https://doi.org/10.1061/\(ASCE\)SU.1943-5428.0000241](https://doi.org/10.1061/(ASCE)SU.1943-5428.0000241).
- Wang, G., J. Welch, T. J. Kearns, L. Yang, and J. Serna. 2015b. "Introduction to GPS geodetic infrastructure for land subsidence monitoring in Houston, Texas, USA." *Proc. Int. Assoc. Hydrol. Sci.* 372 (Nov): 297–303. <https://doi.org/10.5194/piahs-372-297-2015>.
- Wang, G., X. Zhou, K. Wang, X. Ke, Y. Zhang, R. Zhao, and Y. Bao. 2020. "GOM20, a stable geodetic reference frame for subsidence, faulting, and sea-level rise studies along the coast of the Gulf of Mexico." *Remote Sens.* 12 (3): 350. <https://doi.org/10.3390/rs12030350>.
- Wang, W., B. Zhao, Q. Wang, and S. Yang. 2012. "Noise analysis of continuous GPS coordinate time series for CMONOC." *Adv. Space Res.* 49 (5): 943–956. <https://doi.org/10.1016/j.asr.2011.11.032>.
- Wenzel, M., and J. Schroter. 2014. "Global and regional sea level change during the 20th century." *J. Geophys. Res.* 119 (11): 7493–7508. <https://doi.org/10.1002/2014JC009900>.
- Wessel, P., W. H. Smith, R. Scharroo, J. Luis, and F. Wobbe. 2013. "Generic mapping tools: Improved version released." *Eos* 94 (45): 409–410. <https://doi.org/10.1002/2013EO450001>.
- Wilks, D. S. 2006. *Statistical methods in the atmospheric sciences*. 2nd ed. Cambridge, MA: Academic.
- Williams, S. D. P. 2008. "CATS: GPS coordinate time series analysis software." *GPS Solut.* 12 (2): 147–153. <https://doi.org/10.1007/s10291-007-0086-4>.
- Williams, S. D. P., Y. Bock, P. Fang, P. Jamason, R. M. Nikolaidis, L. Prawirodirdjo, M. Miller, and D. J. Johnson. 2004. "Error analysis of continuous GPS position time series." *J. Geophys. Res.* 109 (B3): B03412. <https://doi.org/10.1029/2003JB002741>.
- Xu, C., and D. Yue. 2015. "Monte Carlo SSA to detect time-variable seasonal oscillations from GPS-derived site position time series." *Tectonophysics* 665 (8): 118–126. <https://doi.org/10.1016/j.tecto.2015.09.029>.
- Yang, L., G. Wang, Y. Bao, T. J. Kearns, and J. Yu. 2016. "Comparisons of ground-based and building-based CORS: A case study in the Puerto Rico and Virgin Islands region." *J. Surv. Eng.* 142 (3): 05015006. [https://doi.org/10.1061/\(ASCE\)SU.1943-5428.0000155](https://doi.org/10.1061/(ASCE)SU.1943-5428.0000155).
- Zervas, C. 2009. *Sea level variations of the United States 1854–2006*. NOAA Technical Rep. NOS CO-OPS 053. Silver Spring, MD: National Oceanic and Atmospheric Administration.

- Zervas, C., S. Gill, and W. Sweet. 2013. *Estimating vertical land motion from long-term tide gauge records*. NOAA Technical Rep. NOS CO-OPS 065. Silver Spring, MD: National Oceanic and Atmospheric Administration.
- Zhang, J., Y. Bock, H. Johnson, P. Fang, S. Williams, J. Genrich, S. Wdowinski, and J. Behr. 1997. "Southern California permanent GPS geodetic array: Error analysis of daily position estimates and site velocities." *J. Geophys. Res.* 102 (B8): 18035–18055. <https://doi.org/10.1029/97JB01380>.
- Zhao, R., G. Wang, X. Yu, X. Sun, Y. Bao, G. Xiao, W. Gan, and S. Shen. 2020. "Rapid land subsidence in Tianjin, China derived from continuous GPS observations (2010–2019)." *Proc. Int. Assoc. Hydrol. Sci.* 382 (Apr): 241–247. <https://doi.org/10.5194/piahs-382-241-2020>.
- Zhou, X., G. Wang, K. Wang, H. Liu, H. Lyu, and M. J. Turco. 2021. "Rates of natural subsidence and submergence along the Texas coast derived from GPS and tide gauge measurements (1904–2020)." *J. Surv. Eng.* 147 (4): 04021020. [https://doi.org/10.1061/\(ASCE\)SU.1943-5428.0000371](https://doi.org/10.1061/(ASCE)SU.1943-5428.0000371).